5-2018

Comparing Disdrometer-measured Raindrop Size Distributions from VORTEX-SE with Distributions from Polarimetric Radar Retrievals Using the Constrained Gamma Method

Jessica Bozell
Purdue University

Follow this and additional works at: https://docs.lib.purdue.edu/open_access_theses

COMPARING DISDROMETER-MEASURED RAINDROP SIZE DISTRIBUTIONS FROM VORTEX-SE WITH DISTRIBUTIONS FROM POLARIMETRIC RADAR RETRIEVALS USING THE CONSTRAINED GAMMA METHOD
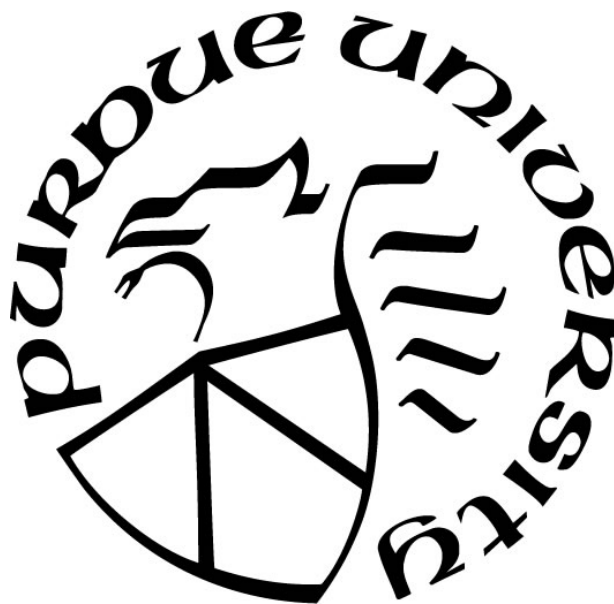
by

Jessica Bozell

A Thesis

Submitted to the Faculty of Purdue University

In Partial Fulfillment of the Requirements for the degree of

Master of Science in Atmospheric Science

Department of Earth, Atmospheric, and Planetary Sciences

West Lafayette, Indiana

May 2018

THE PURDUE UNIVERSITY GRADUATE SCHOOL
STATEMENT OF COMMITTEE APPROVAL

Dr. Daniel T. Dawson II, Chair

    Department of Earth, Atmospheric, and Planetary Sciences

Dr. Alexander Gluhovsky

    Department of Earth, Atmospheric, and Planetary Sciences

Dr. Robin Tanamachi

    Department of Earth, Atmospheric, and Planetary Sciences

Approved by:

    Dr. Darryl Granger

        Head of the Graduate Program

ACKNOWLEDGMENTS

TABLE OF CONTENTS

LIST OF TABLES

LIST OF FIGURES

ABSTRACT

Author: Bozell, Jessica, M. MS
Institution: Purdue University
Degree Received: May 2018
Title: Comparing Disdrometer-measured Raindrop Size Distributions from VORTEX-SE with Distributions from Polarimetric Radar Retrievals Using the Constrained Gamma Method
Major Professor: Daniel T. Dawson II

Many aspects of microphysical variations within supercells are not well understood, even though they play a key role in storm dynamics and evolution. Raindrop size distributions (DSDs) provide a lot of insight into a storms microphysics, however, DSDs vary significantly throughout storms. Unfortunately, current radars do not have the capability to directly observe DSDs, making retrieval algorithms based on advanced microphysical models and in-situ disdrometer observations necessary. If these small-scale variations can be better characterized, and differences between convective regimes quantified, it will lead to improved algorithms for retrieving DSD parameters from radars as well as improved microphysical parameterizations within numerical weather prediction models. With better modeling of supercells, tornado predictions and warnings can be improved.

While disdrometers can directly measure DSDs, they are severely limited in spatial coverage. In order to improve our understanding of the spatial variation of DSDs across supercells, radar retrieval methods, such as the constrained-gamma method, can be used to retrieve DSD parameters at high spatial resolution across an entire storm. The constrained-gamma method works by finding a relationship between the shape parameter μ and the slope parameter Λ of the underlying gamma distribution. In this study, the constrained gamma method is applied to radar data collected during the 2016 and 2017 VORTEX-SE field program in order to retrieve gamma distributions from polarimetric radar variables. Specifically, new μ-Λ relations will be derived from VORTEX-SE disdrometer data and will be compared to μ-Λ relations found in other studies. The utility of retrievals will then be evaluated using the different relations for characterizing the spatiotemporal variation of DSDs for VORTEX-SE storms. To further improve the μ-Λ relation, the effects of measurement errors will be minimized by using a sorting and averaging technique to group DSDs with similar microphysical properties together.

1. INTRODUCTION

Knowledge of raindrop size distributions (DSDs) is critical to understanding the microphysics of convective storms, and the information they provide can have many useful applications. DSDs can vary widely both within storms and between storms in different environments. Within storms, microphysical processes such as collision, coalescence, drop breakup, and evaporation can lead to varying DSD shapes (Kalina et al. 2014). Changes in DSD shape and size influence properties and processes of storms such as the structure and behavior of downdrafts, precipitation rates, and the development of the cold pool (e.g., Gilmore et al. 2004; Snook and Xue 2008; Dawson et al. 2010, 2015, 2016; Dawson and Romine 2011; Friedrich et al. 2013; Kumjian et al. 2015). These processes are critical when assessing the tornado potential of severe storms (Snook and Xue 2008; Dawson et al. 2015, 2016). Unfortunately, they occur below radar measurement levels, making it very difficult to observe these microphysical changes within storms. Because of this, radar retrievals based on in-situ DSD observations are necessary to investigate these small scale variations (Haddad et al. 1997; Bringi et al. 2002, 2003; Gorgucci et al. 2002; Brandes et al. 2004a, b; Vivekanandan et al. 2004; Zhang et al. 2001, 2006; Cao et al. 2008). Better understanding of microphysical properties of storms will enhance storm modeling, which in turn will improve tornado predictions and warnings.

The Southeastern United States experiences a disproportionately large number of cold season and nocturnal tornadoes as compared to the rest of the country (Ashley 2007; Guyer and Dean 2010). This is thought to be related to the fact that tornadoes in the Southeast are more likely to occur in low cape, high shear environments (Schneider et al. 2006; Sherburn and Parker 2014; Davis and Parker 2014). Nocturnal tornadoes are more likely to result in deaths, as they are more difficult to spot and most people are asleep at this time. Cold season tornadoes are also more likely to be deadly because they occur at a time of the year when the public is not prepared for severe weather (Ashley 2007; Ashley et al. 2008). These uncommon tornado environments combined with the complex terrain of the Southeast have resulted in the southeast having a higher number of deadly tornadoes. Because of these factors, researchers believe that there are important differences in Southeast thermodynamic environments, as compared to those of more well studied regions such as the Great Plains, which impact tornado potential. As previously mentioned, thermodynamic differences can arise from microphysical variations, thus creating a need to

investigate the microphysical differences between Southeast tornado environments and Great Plains environments. The Verification of the Origins of Rotation in Tornadoes Experiment-Southeast (VORTEX-SE) is focused on studying the factors that affect the formation, intensity, structure, and path of tornadoes in the Southeast (Rasmussen et al. 2015). Understanding how potentially tornadic deep convection in the southeast may differ microphysically from other storm environments is another overarching goal of the project. High quality in-situ observations of DSDs in the Southeast combined with polarimetric radar data will aid in the understanding of microphysical variability impacts on storm dynamics and tornado potential in the region.

In this paper, a previously established DSD retrieval method will be used to estimate microphysical parameters across entire storms during VORTEX-SE cases from polarimetric radar data, and the results will be compared to *in-situ* disdrometer observations. In Chapter 2, a comprehensive background on DSD fitting, parameter estimation, and retrieval methods is provided. The disdrometer and radar data used for the analyses are then described in Chapter 3. Chapter 4 provides the details of the methodology used in this research. The results are presented in Chapter 5, detailing both the overall results from the entire data set and the results from three specific case studies during VORTEX-SE. Finally, Chapter 6 summarizes the findings of the paper.

2. BACKGROUND

a. DSD Fitting

In order to retrieve DSDs from polarimetric radar data, a fitting procedure must first be selected to model the observed DSD. DSDs were originally thought to be described by the exponential distribution, expressed by the parameters N_0 and Λ (Marshall and Palmer 1948; Laws and Parsons 1943). The distribution parameters could then be derived from Z and Z_{DR} or attenuation (Seliga and Bringi 1976; Ulbrich 1983). While DSDs do tend towards the exponential distribution over long periods of time, it has been found that over shorter sampling periods, the exponential distribution does not sufficiently describe the observed DSD shape. Over short periods of time, the exponential distribution tends to overestimate the number of very small and very large drops (Vivekanandan et al. 2004). Ulbrich (1983) thus suggested using the gamma distribution of the form

$$N(D) = N_0 D^{\mu} \exp(-\Lambda D), \tag{1}$$

where $N(D)$ (mm^{-1} m^{-3}) is the drop size distribution, N_0 (mm$^{-1-\mu}$ m^{-3}) is an intercept parameter, μ is a distribution shape parameter, Λ (mm^{-1}) is a slope parameter, and D (mm) is the sphere-equivalent volume diameter. Because the gamma distribution has three parameters, it can model a wider range of DSDs, better describing the natural variations in DSD shape (Ulbrich 1983).

b. DSD Parameter Estimation

Once a functional form has been chosen to model the observed DSD, a method for estimating the parameters needs to be selected. Estimation methods include the method of moments (Ulbrich 1983), maximum-likelihood, and L-moment estimators (Kliche et al. 2008). Thurai et al. (2014) found that all three methods performed similarly for estimates of μ and Λ, while Cao and Zhang (2009) found that the maximum-likelihood and L-moment methods performed poorly when the observed DSD deviated from the gamma fit. Because of this, the method of moments is the estimator most widely used to retrieve DSD parameters.

i. Method of Moments

The method of moments uses the observed DSD to estimate the statistical moments through the following equation from Ulbrich (1983):

$$M_n = \int_0^\infty D^n N(D)dD = N_0 \Lambda^{-(\mu+n+1)} \Gamma(\mu+n+1) \qquad (2)$$

where M_n is the nth moment of the DSD. The other parameters follow as those described in Eq. (1). Three moments are then used to create a system of equations to solve for the three unknown DSD parameters. Following the equations of Ulbrich and Atlas (1998), the second, fourth, and sixth moments can be used to form a ratio of the moments, η, to eliminate N_0 and Λ:

$$\eta = \frac{M_4^2}{M_2 M_6} = \frac{(3+\mu)(4+\mu)}{(5+\mu)(6+\mu)}. \qquad (3)$$

This moment ratio can now be solved for μ:

$$\mu = \frac{(7-11\eta) - [(7-11\eta)^2 - 4(\eta-1)(30\eta-12)]^{1/2}}{2(\eta-1)}. \qquad (4)$$

Λ is then found from

$$\Lambda = \left(\frac{M_2(3+\mu)(4+\mu)}{M_4} \right)^{1/2} \qquad (5)$$

and finally, N_0 can be found by plugging μ from Eq. (4) and Λ from Eq. (5) back into any of the moment equations. N_0 is calculated from the sixth moment in the following equation:

$$N_0 = \frac{M_4 \Lambda^{5+\mu}}{\Gamma(5+\mu)}. \qquad (6)$$

Once the three gamma DSD parameters are estimated, the rest of the physical parameters can be calculated.

ii. Truncated Method of Moments

The method of moments presented above assumes that the moment integrals extend over all possible diameters, from 0 to ∞, but this assumption can lead to significant errors in parameter estimations (Ulbrich and Atlas 1998). In reality, drops are being observed over a finite interval, from D_{min} (mm) to D_{max} (mm), and a truncated method of moments can be used to integrate over only the observed drop size range (Cao et al. 2008; Vivekanandan et al. 2004). Effects of truncation at small diameters are typically negligible, but at large diameters, ignoring the effects of truncation can result in overestimations of μ, which will then lead to the overestimation of the other parameters. Truncation at large diameters can occur because of things such as instrumental truncation or systematic drop size sorting (Ulbrich and Atlas 1998).

The truncated method of moments (TMF) follows a similar process to the untruncated method of moments, but now the integral extends from D_{min} to D_{max}, requiring the use of the incomplete gamma function, γ(…). The below TMF procedure follows that of Vivekanandan et al. (2004):

$$
M_{TMF,n} = \int_{D_{min}}^{D_{max}} D^n N(D)dD
$$
$$
= N_0 \Lambda^{-(\mu+n+1)}[\gamma(\mu + n + 1, \Lambda D_{max} - \gamma(\mu + n + 1, \Lambda D_{min})]. \tag{7}
$$

The truncated moment ratio, η_{TMF}, is used to eliminate N_0 from the expression, with the second, fourth, and sixth moments again being used as an example. As seen below, it is now much more difficult to separate the dependence of μ_{TMF} and Λ_{TMF} (Thurai et al. 2014):

$$
\eta_{TMF} = \frac{[\gamma(5 + \mu_{TMF}, \Lambda_{TMF}D_{max}) - \gamma(5 + \mu_{TMF}, \Lambda_{TMF}D_{min})]^2}{\gamma(3 + \mu_{TMF}, \Lambda_{TMF}D_{max})\gamma(7 + \mu_{TMF}, \Lambda_{TMF}D_{max}) - \gamma(3 + \mu_{TMF}, \Lambda_{TMF}D_{min})\gamma(7 + \mu_{TMF}, \Lambda_{TMF}D_{min})}. \tag{8}
$$

Because of this, an iterative approach has to be used to adjust μ_{TMF} and Λ_{TMF} until the truncated moment ratio converges to the observed moment ratio. The method of moments μ and Λ are used to initialize the μ_{TMF} and Λ_{TMF} values, and then Λ is solved by

$$
\Lambda_{TMF} = \left\{ \frac{M_{TMF,2}[\gamma(5 + \mu_{TMF}, \Lambda_{TMF}D_{max}) - \gamma(5 + \mu_{TMF}, \Lambda_{TMF}D_{min})]}{M_{TMF,4}[\gamma(3 + \mu_{TMF}, \Lambda_{TMF}D_{max}) - \gamma(3 + \mu_{TMF}, \Lambda_{TMF}D_{min})]} \right\}^{1/2}. \tag{9}
$$

$N_{0,TMF}$ can then be solved in the same way as the untruncated method of moments, by plugging μ_{TMF} and Λ_{TMF} into any of the truncated moment expressions (Ulbrich 1985; Vivekanandan et al. 2004; Thurai et al. 2014).

iii. Moment Selection

When using the method of moments, it is important to consider which three moments will be most beneficial to use in the DSD parameter estimations. Common combinations include M246 (Ulbrich and Atlas 1998; Zhang et al. 2001, 2003; Brandes et al. 2004a, b; Vivekanandan et al. 2004) and M346 (Kozu and Nakamura 1991; Tokay and Short 1996; Tokay et al. 2001). Some of the first studies done analyzing the errors associated with the estimated moments found that the higher order DSD moments have higher errors (Gertzman and Atlas 1977; Wong and Chidambaram 1985). This is because large drops weigh more heavily in the calculation of higher-order moments (Cao et al. 2008), and since large drop sizes are likely to have larger sampling errors (Chapter 3a), it results in larger errors for the estimated moments. However, the higher-order moments are better correlated with radar measurements, making them still useful in radar retrievals (Cao and Zhang 2009). Middle-order moments, such as moments two and three, tend to have the lowest errors (Cao et al. 2008). Looking at sampling error correlations between DSD moments, it was found that the further apart two moments are, the smaller their error correlation (Zhang et al. 2003; Cao et al. 2008). Overall, the various moment estimator sets perform similarly, with the M234 estimator resulting in the smallest errors, but only if the observed DSD follows the gamma distribution fit closely (Smith et al. 2005; Cao and Zhang 2009). However, if the observed DSD deviates from the gamma fit, the M234 estimator performs more poorly. Therefore, it is suggested that the selection of moments is based on which estimated parameters are of most relevance to the research. In DSD retrieval methods, higher-order parameters such as Z_H and Z_{DR} are of great interest, making the M246 estimator set a popular choice (Cao and Zhang 2009).

c. DSD Parameter Radar Retrievals

Because there are three governing parameters of the gamma DSD, three remote measurements or relations are needed to retrieve the gamma DSD parameters from radar data. It has been shown that the three parameters of the gamma DSD are mutually dependent (Ulbrich 1983; Chandrasekar and Bringi 1987; Haddad et al. 1997; Kozu and Nakaura 1991). This mutual dependence makes it more difficult to separate true physical correlations from those arising from statistical error (Haddad et al. 1997). However, if physical correlations can be proven, a relation between two parameters could then be used to reduce the number of unknowns in the DSD retrieval, making retrievals possible from a pair of remote measurements (Zhang et al. 2003; Brandes et al. 2004a). As discussed in Zhang et al. (2003) and Cao et al. (2008), Ulbrich (1983) first attempted to use a N_0-μ relation to retrieve the DSD parameters from radar reflectivity and attenuation. This relationship was then determined to be a result of statistical error by Chandrasekar and Bringi (1987). Bringi et al. (2002) and Gorgucci et al. (2002) then attempted to use radar measurements of Z_H, Z_{DR}, and K_{DP} to retrieve the DSD parameters. However, K_{DP} is often noisy and can result in large variations in retrieved parameters (Brandes et al. 2004a).

High correlations have been found between μ and Λ, leading to the development of the μ-Λ relation and the so-called constrained-gamma method (Zhang et al. 2001; Brandes et al. 2004a; Cao et al. 2008). An empirical, constraining relation between μ and Λ can be used along with radar measured Z_H and Z_{DR} to retrieve the DSD parameters (Zhang et al. 2001; Brandes et al. 2004a). Chandrasekar and Bringi (1987) expressed concerns about whether the relation was caused by sampling errors or if it was an actual physical relation, but Zhang et al. (2003) demonstrated that the μ-Λ relation was separate from the linear relation of the sampling errors and therefore was uninfluenced by statistical error. The existence of a μ-Λ relation would suggest that there is also a relationship between mean mass weighted diameter (D_m) and mass spectrum width (σ_m), as both of these parameters are uniquely determined from μ and Λ (Brandes et al. 2004b). Because σ_m and D_m are physical parameters that can be directly calculated from the observed DSD, they can be used to test the validity of the μ-Λ relation. If the μ-Λ relation accurately describes rain physics, then the observed σ_m-D_m relation should match the σ_m-D_m relation derived from the μ-Λ relation (Cao et al. 2008).

It is thought that the μ-Λ relation may depend on the climate type, storm type, and state of the storm (Zhang et al. 2003; Atlas and Ulbrich 2006; Cao et al. 2008). Previous studies in the Great Plains and subtropics have derived slightly different μ-Λ relations, signifying that the μ-Λ relation may be impacted by changes in precipitation mechanisms (Zhang et al. 2001; Brandes et al. 2004a, b). It is possible that creating specific μ-Λ relations for different climatic regions will improve the overall accuracy of radar retrievals. In an attempt to customize the μ-Λ relation based on storm type and state, Cao et al. (2008) used an adjustment term in the μ-Λ relation based on radar reflectivity to improve their retrieval results in high Z_{DR}, low Z_H regions. Brandes et al. (2003) used the truncated moment fit to derive their μ-Λ relation to improve retrievals in areas of high rain rate.

i. DSD Sorting and Averaging based on Two Parameters

When trying to validate the existence of a μ-Λ relation, it can be difficult to separate the sampling errors from the real physical variation, especially when the DSDs are being measured by a single disdrometer (Cao et al. 2008). Because of this, attempts have been made to create averaging techniques that would average together DSDs that had similar physical properties, to reduce the DSD variability and sampling errors. The first attempt at this was done by Lee and Zawadzki (2005). They created the sequential intensity filtering technique (SIFT) which would sort DSDs during a certain event by reflectivity, and then average neighboring DSDs together. While this did help to reduce the sampling error, it also reduced the physical relations between parameters. Two DSDs can have similar reflectivities while also representing very different DSD shapes and underlying DSD properties. Cao et al. (2008) then introduced the sorting and averaging method based on two parameters (SATP) in an effort to preserve the shape and slope of DSDs, while still being able to reduce the sampling error. The SATP method introduced the ability to sort the DSDs by two parameters instead of one, and was also applicable to an entire dataset, rather than just one specific timeframe. It was suggested that R (rain rate) and D_0 (median volume diameter) be used to sort the DSDs, as these represent the middle moments, which are most accurately measured by disdrometers. A finely scaled 2-D grid is created, and DSDs with similar R and D_0 values are averaged together to create new DSDs, from which a μ-Λ relation less biased by sampling error can be created.

3. DATA

a. Disdrometer Data

i. Data Collection

For this study, four Portable In-situ Precipitation Stations (PIPS), pictured in Figure 1, were utilized during the 2016 and 2017 VORTEX-SE field campaigns. Each PIPS consists of an OTT Parsivel[2] (Particle Size and Velocity) laser disdrometer (Löffler-Mang and Joss 2000; Tokay et al. 2014), along with sensors to measure temperature, relative humidity, pressure, and wind. The Parsivel disdrometer can detect diameters between 0.25 and 25 mm and velocities of up to 20 ms^{-1}. The lowest two diameter bins are left empty due to a low signal-to-noise ratio, resulting in drops with diameters of less than 0.25 mm being ignored by the disdrometer (Tokay et al. 2013). The disdrometer produces a horizontal sheet of infrared light (160 mm x 30 mm), and when particles pass through the beam, there is a reduction of voltage which is measured by the instrument. The reduction signal is then inverted, amplified, and smoothed. The maximum amplitude of the signal reduction is used to measure the particle diameter, while the length of time that the signal is reduced is used to measure the velocity. The Parsivel software then uses 32 non-equidistant size and fall-speed bins to sort each particle, as shown in Figure 2. The particle is assigned the diameter and velocity that corresponds to the bin center (Löffler-Mang and Joss 2000). It is assumed that only one particle is passing through the beam at a time (Raupach and Berne 2015).

Figure 1. A photograph of two PIPS, complete with disdrometers and weather sensors. The Parsivel[2] disdrometers are circled in red.

One of the advantages of the Parsivel[2] disdrometer is that it is low cost, robust, and easy to handle, making it ideal for rapidly deploying multiple instruments in the path of a storm (Löffler-Mang and Joss 2000; Friedrich et al. 2013). However, Parsivel disdrometers are prone to measurement errors of small and large drop concentrations (Raupach and Berne 2015; Tokay et al. 2013; Park et al. 2017). Between the 5-10 mm diameter range, bin widths are 1 mm, leading to larger uncertainty at these diameters. Overestimations of large drop number concentrations can occur during heavy rainfall, as it is more likely that multiple particles fall through the beam at one time and are misclassified as large drops (Thurai et al. 2011; Tokay et al. 2013). Parsivel disdrometers struggle with accurate small drop number concentrations because of instrument resolution and reduced sensitivity (Thurai et al. 2014). Despite these disadvantages though, Thurai et al. (2011) found that the Parsivel[2] disdrometer has comparable performance to the higher resolution 2D-video disdrometers when $R < 20$ mm h^{-1}. For higher rain rates, they found that the Parsivel disdrometer tends to measure higher rain parameter values, although the times of largest disagreement corresponded with times where hail or graupel were observed.

The 2016 and 2017 VORTEX-SE field campaigns occurred from 25 March-1 May each year. In 2017, PIPS 2A was collocated with the U-Mass FMCW (PIPS FMCW) for the duration of the project. PIPS FMCW was positioned approximately 27.5 km southeast of the Huntsville, AL (KHTX) WSR-88D radar, with the radar beam scanning 0.28 km above the instrument. To distinguish between days with and without rainfall, data were discarded if the disdrometer measured Z never exceeded 20 dBZ, as this is the approximate threshold between drizzle and light rain (Rinehart 2004). Methods for deriving polarimetric variables from the disdrometer data are discussed in Chapter 4c. Overall, 15 rainy days were observed by the PIPS FMCW and are used in the data analysis. A majority of these systems were quasi-linear convective systems (QLCS), with only four of the events being cellular in nature. In addition to the PIPS FMCW data, three intensive operating periods (IOPs) from 2016 and six IOPs from 2017 are used. The details for each IOP used in the analysis are listed in Table 1. As seen from the table, five of the IOPs were conducted during QLCS events, while the other four IOPs observed multicellular clusters. Tornadoes or tornado warnings were associated with IOPs 3, 4C-2016, and 4C-2017. In Chapter 5, IOPs 4B, 4C-2016, and 4C-2017 are used for individual case studies. The overall data set consists of 4215 1-min DSDs. Previous studies have used as few as 1341 1-min samples (Vivekanandan et al. 2004) or as many as 14200 1-min DSD samples (Cao et al. 2008).

Table 1. Descriptions of the VORTEX-SE IOPs used in the analysis.

	Date	Time (UTC)	PIPS	Storm Type	Radar Distance and Height
IOP 3	31-May-2016	2156-2356	PIPS 1A, 1B, 2A, 2B	Supercell clusters	d = 138.7 km h = 2.34 km
IOP 4B	29-Apr-2016	2124-2357	PIPS 1B, 2A, 2B	QLCS	d = 63.8 km h = 0.80 km
IOP 4C	30-Apr-2016	1933-2139	PIPS 1B, 2A, 2B	Supercell clusters	d = 111.9 km h = 1.71 km
IOP 1A	25-Mar-2017	1711-1856	PIPS 1A, 1B, 2B	QLCS	d = 115.8 km h = 1.80 km
IOP 1B	27-Mar-2017	1951-2222	PIPS 1A	Supercell clusters	d = 133.2 km h = 2.21 km
IOP 1B-2	28-Mar-2017	0121-0330	PIPS 1A, 1B, 2B	QLCS	d = 130.4 km h = 2.14 km
IOP 3B	15-Apr-2017	2303-0031	PIPS 1B	Supercell clusters	d = 48.2 km h = 0.56 km
IOP 4A	27-Apr-2017	0455-0743	PIPS 1A, 1B	Dissipating QLCS	d = 139.4 km h = 2.36 km
IOP 4C	30-Apr-2017	1829-2009	PIPS 1A, 1B, 2B	QLCS	d = 120.0 km h = 1.90 km

ii. Data Filtering

In order to perform high-quality retrievals with the disdrometer observations, the data first need to be filtered to classify and remove suspicious particles. Following the procedures of Kalina et al. (2014) and Friedrich et al. (2013), a hydrometeor classification scheme is used to distinguish rain particles from graupel, hail, and ice particles. The classification scheme is pictured in Figure 2. Because rain drops are assumed to have $D < 8$ mm, all drops larger than this can be removed (Friedrich et al. 2013). The hydrometeor classification, which is based on disdrometer diameter ranges and fall speed-diameter relations, is then used to remove any remaining hail or graupel particles. Once all non-rain particles are removed, the data is filtered to eliminate DSDs that were likely contaminated by strong winds, splashing drops, and margin falling drops. All of these scenarios result in drops with unrealistic fall speeds and diameters (Friedrich et al. 2013). Strong winds of over 20 ms^{-1} have been found to result in large drops ($D > 5$ mm) being recorded at fall speeds of less than 1 ms^{-1}. Since those are unrealistically low fall speeds for drops of that size, all time steps where this occurs are removed. Splashing drops occur when particles hit the surface of the PIPS instrument and break into smaller drops before then falling back through the disdrometer beam, resulting in small drops with very low fall speeds. "Margin fallers" occur when drops fall

through the edge of the beam, and result in small drops with very high fall speeds. To remove splashing drops and margin fallers, all drops with a fall speed 60% faster or slower than the fall-speed diameter relationship would suggest are removed (Gunn and Kinzer 1949; Atlas et al. 1973; Friedrich et al. 2013).
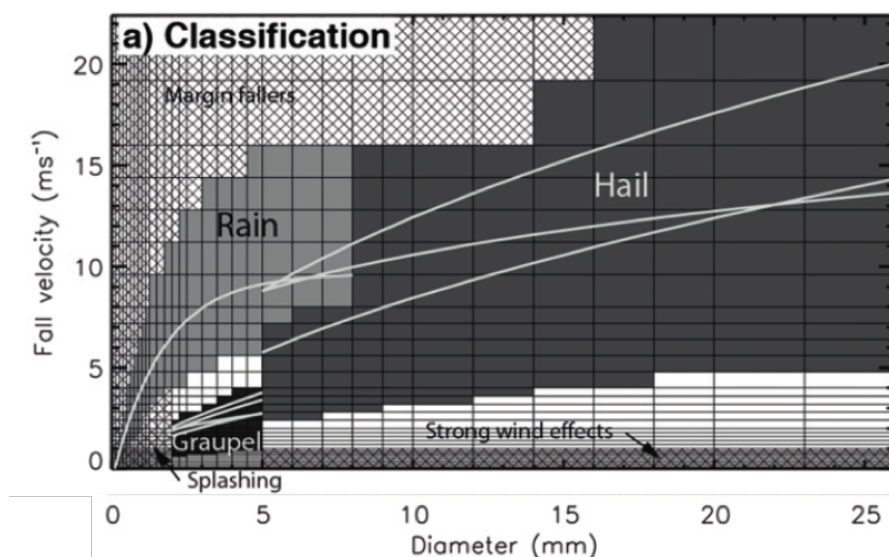
Figure 2. A visual representation of the hydrometeor classification scheme used to separate rain drops from other particles, based on fall-speed and diameter. Regions that are filtered out due to various sampling errors are also highlighted. Originally Figure 5a in Friedrich et al. 2013.

b. Radar Data

S-band radar data is used for comparison with PIPS observations during the VORTEX-SE deployments. Level 2 radar data is collected from either the KHTX (Huntsville, AL) or the KGWX (Columbus Air Force Base, MS) WSR-88D radars, depending on which was closest to the PIPS. The lowest elevation angle of 0.5° is used for radar analysis. When processing the radar observations for comparison with the disdrometer observations, the closest radar gate to the disdrometer is located by finding the shortest Euclidean distance from the disdrometer location to the center of the radar gate. The Cressman (1959) scheme then uses a non-zero weighting function to smooth radar gates within 1 km of the disdrometer location. The radar observations are then re-indexed by interpolation in order to create an array of estimated radar measurements that occurred at the same time as the disdrometer measurements for comparison. All radar measurements with $\rho_{HV} < 0.9$ are removed, to eliminate non-rain precipitation echoes from the radar data.

Even with the quality controls set into place, measurement differences between the disdrometer and radar are still certain to occur, limiting the overall accuracy of radar retrievals. Growth and evaporation of raindrops is one potential source of disagreement between the radar and disdrometer. As the raindrops fall from the radar beam to the disdrometer beam, it is likely that the DSD is changing, as drops can grow in size, break-up into smaller drops, or evaporate completely, resulting in different DSDs being observed by the two instruments. The strength of the low-level winds can also play an important role, as strong low-level winds can advect the drops downstream of the disdrometer, again causing the two instruments to observe different DSDs. Related to both of these issues is radar beam height. The higher the radar beam is scanning above the disdrometer, the greater the distance over which the DSDs have time to change (Kalina et al. 2014). The temporal and spatial scales of both instruments can also produce disagreement between the results. It typically takes a radar 5-8 minutes to complete one full volume scan, while the disdrometer is measuring distributions every 10 s. Radar sampling volumes can also be 10^7 times greater than a disdrometer's sampling volume (Cao et al. 2008).

4. METHODS

The disdrometer and corresponding radar data were analyzed using the Python programming language. Disdrometer measured reflectivity time series that do not reach above 20 dBZ are discarded as non-rain days. The disdrometer data is processed, and the strong wind DSDs and drops that are suspected of being splashing drops or margin fallers are masked out. DSD observations are then resampled from 10 s to 1 min. Afterwards, any DSD bins where no rain drops are recorded are masked out.

Next, the observed DSDs are fit with the exponential and gamma distributions using the method of moments. Moments zero through six are estimated using the equation

$$M_n = \sum D^n N(D) \Delta D \qquad (10)$$

to sum across all of the bins of the observed DSD. In the equation, D (mm) is the average drop size of the bin, $N(D)$ (mm^{-1} m^{-3}) is the observed DSD, and ΔD (mm) is the width of the bin. The observed physical parameters are then calculated. Rain rate [R, mm hr^{-1}] is calculated using the Brandes et al. (2002) equations:

$$R = 6\pi * 10^{-4} \sum D^3 [mm^3] v(D)[m\ s^{-1}] N(D)[m^{-3}mm^{-1}]\Delta D[mm] \qquad (11)$$

where

$$v(D) = -0.1021 + 4.932D - 0.9551D^2 + 0.07934D^3 - 0.002362D^4. \qquad (12)$$

Equations for the remaining physical parameters are taken from Brandes et al. (2004a). Liquid water content [W, g m^{-3}] is given by the expression

$$W = \frac{\pi}{6} * M_3 * 1000, \qquad (13)$$

total number concentration [N_T, m^{-3}] is equal to the zeroth-moment

$$N_T = \sum N(D)\Delta D, \tag{14}$$

and median volume diameter [D_0, mm], the diameter for which half of the liquid water content is above and below it, is defined as

$$\int_0^{D_0} D^3 N(D)dD = \int_{D_0}^{D_{max}} D^3 N(D)dD. \tag{15}$$

a. Exponential and Gamma Distribution Fitting

Based on Zhang et al. (2008), the exponential distribution parameters are calculated using the third and sixth moments of the DSD. The slope parameter [Λ, mm^{-1}] is first calculated by the equation

$$\Lambda = \frac{M_x \Gamma(y+1)}{M_y \Gamma(x+1)}^{1/(y-x)} \tag{16}$$

where x is equal to three and y is equal to six, for the third and sixth moments. Once Λ is calculated, the intercept parameter [N_0, m^{-3} mm^{-1}] can be found by the equation

$$N_0 = \frac{M_x \Lambda^{x+1}}{\Gamma(x+1)}. \tag{17}$$

The intercept and slope parameters are then used to calculate the exponential distribution fit to the observed DSD

$$N(D)_{exp} = N_0 \exp(-\Lambda D). \tag{18}$$

The gamma distribution parameters (N_0, μ, and Λ) are then calculated using the second, fourth, and sixth moments, as described in Chapter 2b Section i. The μ and Λ are then used to initialize the truncated moment fit. D_{max} is found from the observed DSD as the midpoint of the largest bin where a raindrop is recorded. The truncated moment fit is performed using Eqs. (7) - (9) and is coded following the Fortran code provided by Guifu Zhang (Personal communication, February 11, 2018). If initially the TMF moment ratio, η_{TMF}, is less than the observed moment ratio, η, η_{TMF} is reduced through an iterative process by subtracting 0.01 from μ_{TMF} until η_{TMF} is greater than η. Once η_{TMF} has converged to η, Λ_{TMF} is found using Eq. (9) and $N_{0,TMF}$ is found using Eq. (6), substituting in μ_{TMF} and Λ_{TMF}. The untruncated and truncated gamma distribution fits can be found by plugging the corresponding DSD parameter set into Eq. (1). The other rain parameters (N_T, W, R, and D_0) are then calculated for both the untruncated and truncated gamma fits (Vivekanandan et al. 2004; Thurai et al. 2014).

b. μ-Λ Relation

A new μ-Λ relation for southeast U.S. storms is computed by using all of the IOP and PIPS FMCW data. An initial relation is formed based on the unfiltered dataset using a second-order polynomial least-square fit, with 4215 individual 1-min DSDs being included in the fit. The results are shown in Figure 3a. The data are then filtered aggressively by masking all data points with R < 5 mm hr^{-1} and N_T < 1000 counts (Figure 3c) in an effort to decrease the effects of sampling errors on the relation. This reduces much of the scatter observed in the μ-Λ pairs, leaving only 437 points, and increases the correlation of the relation (Zhang et al. 2003; Vivekanandan et al. 2004). To improve the accuracy of the μ-Λ relation without filtering out a large majority of the data, the SATP method and truncated moment fit are used to derive a third μ-Λ relation (Cao et al. 2008).

A two-dimensional grid is built from R and D_0, with the R grid boxes starting at 0.1 mm hr^{-1} and then incrementally increasing by 10%, and the D_0 grid boxes starting at 0 mm and increasing by intervals of 0.05 mm. All of the observed DSDs are placed into grid boxes based on their observed physical properties, and then all DSDs in each grid box are averaged (Figure 4). This creates a new set of DSDs with reduced sampling errors that still represent the natural DSD variations. The averaged DSDs are then fit with gamma distributions using the truncated moment fit, and the DSD parameters are calculated. A new mean μ-Λ relation is then derived. The original μ-Λ relation is dominated by the low rain rate values, leading to a higher slope in the unfiltered

relation, as lower rain rates coincide with large μ and Λ values. The SATP derived relation gives equal weight to each *R-D₀* set, giving this relation the added advantage of not being largely influenced by any particular rain rate and median volume diameter.

c. Polarimetric Parameter Estimation

Using the process outlined in Zhang et al. (2001), polarimetric variables are calculated from the disdrometer observations and also from each of the distribution fits. The T-matrix technique (Watermann 1969; Ishimari 1991; Vivekanandan et al. 1991; Jung et al. 2008, 2010) is used to look up the scattering amplitudes, which are then used to calculate the rain backscattering amplitudes. The backscattering amplitudes are used in conjunction with each of the *N(D)* distributions to calculate the polarimetric variables. As described in Brandes et al. (2004a), $Z_{H,V}$ (mm^6 m^{-3}) can be determined from the distribution using

$$Z_{H,V} = \frac{4\lambda^4}{\pi^4 |K_w|^2} \int_{D_{min}}^{D_{max}} |f_{HH,VV}(D)|^2 N(D) dD, \tag{19}$$

where $f_{HH,VV}(D)$ are the backscattering amplitudes of a drop at horizontal and vertical polarizations, respectively, K_w is the dielectric factor of water, and λ (mm) is the radar wavelength. Once Z_H and Z_V have been determined from the distribution, Z_{DR} (dB) can be calculated as

$$Z_{DR} = 10\log\left(\frac{Z_H}{Z_V}\right). \tag{20}$$

The correlation coefficient, ρ_{HV}, is solved by

$$\rho_{HV} = \frac{Z_{HV}}{\sqrt{Z_H Z_V}}. \tag{21}$$

d. Radar Retrievals

Before performing the radar retrieval, non-precipitation echoes are removed from the radar observations by masking times where $\rho_{HV} < 0.9$. The interpolation and re-indexing method from Chapter 3b is then applied to the radar observed Z and Z_{DR}. Another mask is then applied to both the radar observed and disdrometer estimated Z and Z_{DR}, masking all times where either set of Z_{DR} rose above 4 dB, as retrievals can become unreliable in high Z_{DR} regions. High Z_{DR} regions often correspond with "big drop" DSDs, which are poorly fit by gamma distributions due to their irregular shape (Brandes et al. 2004a). The retrieval is first performed with the disdrometer estimated Z and Z_{DR} to verify that the retrieval methods produce reasonable results. The radar observations are then used to perform the retrieval.

The retrieval method begins by verifying that the Z and Z_{DR} values are greater than zero. Following the suggestion of Brandes et al. (2004a), empirical relations from Cao et al. (2008) are used to estimate the rain parameters when $Z_{DR} < 0.1$ dB. Following the retrieval method outlined in a Matlab code by Guifu Zhang, the retrieval utilizes an iterative method to run through possible Λ values between 0.1-30 for Z_{DR} between 0.1-4 dB. For each Λ value, μ is estimated from the selected μ-Λ relation. The μ-Λ pair is then used to derive an estimated Z_{DR} value, and the iteration continues until the estimated Z_{DR} converges with the observed Z_{DR} value. Once the best fitting μ-Λ pair has been found, the definition of Z_H can then be used to estimate N_0. The estimated distribution and other rain parameters are then calculated. All retrieved parameters are then masked for Λ values greater than 20, as these values are likely due to measurement errors (Zhang et al. 2003).

5. RESULTS

a. Overall Results

i. Deriving a new μ-Λ relation

Before radar retrievals are performed on the data set, a μ-Λ relation is derived from the observations. Initially, a relation is derived using the entire data set, with no filtering based on rain rate or total drop count (Fig. 3a). Another relation is then formed using the same data, but with the μ_{TMF} and Λ_{TMF} (Fig. 3b). Without data filtering, both distributions exhibit large amounts of spread in the observed μ and Λ values, although the TMF does result in less scatter than the untruncated fit. Reductions in average μ and Λ values are observed when using TMF. This trend was also observed by Vivekanandan et al. (2004). This suggests that the TMF is fitting broader distributions for DSDs of low rain rate, reducing the number of large μ and Λ values. The data set is then filtered to remove all points $R < 5$ mm h^{-1} and total counts < 1000, as this is expected to reduce the effects of sampling errors on the relation (Vivekanandan et al. 2004; Zhang et al. 2003; Brandes et al. 2003). The results, displayed in Figures 3c and 3d, show that the amount of scatter in the points is significantly reduced. The number of points used to derive the relation drops from 4,215 to 437. The average μ and Λ values are greatly reduced, now that the high rain rates dominate the relation. The relations derived from Cao et al. (2008) and Zhang et al. (2001) are plotted alongside the new relations in each plot (hereafter the "Cao" and "Zhang" relations, respectively). The Cao relation was derived from observed rainfall in Oklahoma, and therefore represents continental precipitation and is dominated by cold rain processes. The Zhang relation was derived from Florida rainfall, which represents maritime precipitation with potentially a greater role for warm rain processes. Warm rain processes tend to result in distributions characterized by larger numbers of small drops as compared to cold rain processes. As is seen in Figure 3, the Zhang relation has a greater slope than the Cao relation, because the large numbers of small drops result in larger magnitudes μ and Λ. In all four cases observed in Fig. 3, the new relation derived from the VORTEX-SE data falls between the continental and maritime rain relations. This suggests that the southeast U.S. is a region that experiences rain DSD characteristics intermediate between the two regimes, being situated near the Gulf of Mexico as well as the Great Plains.
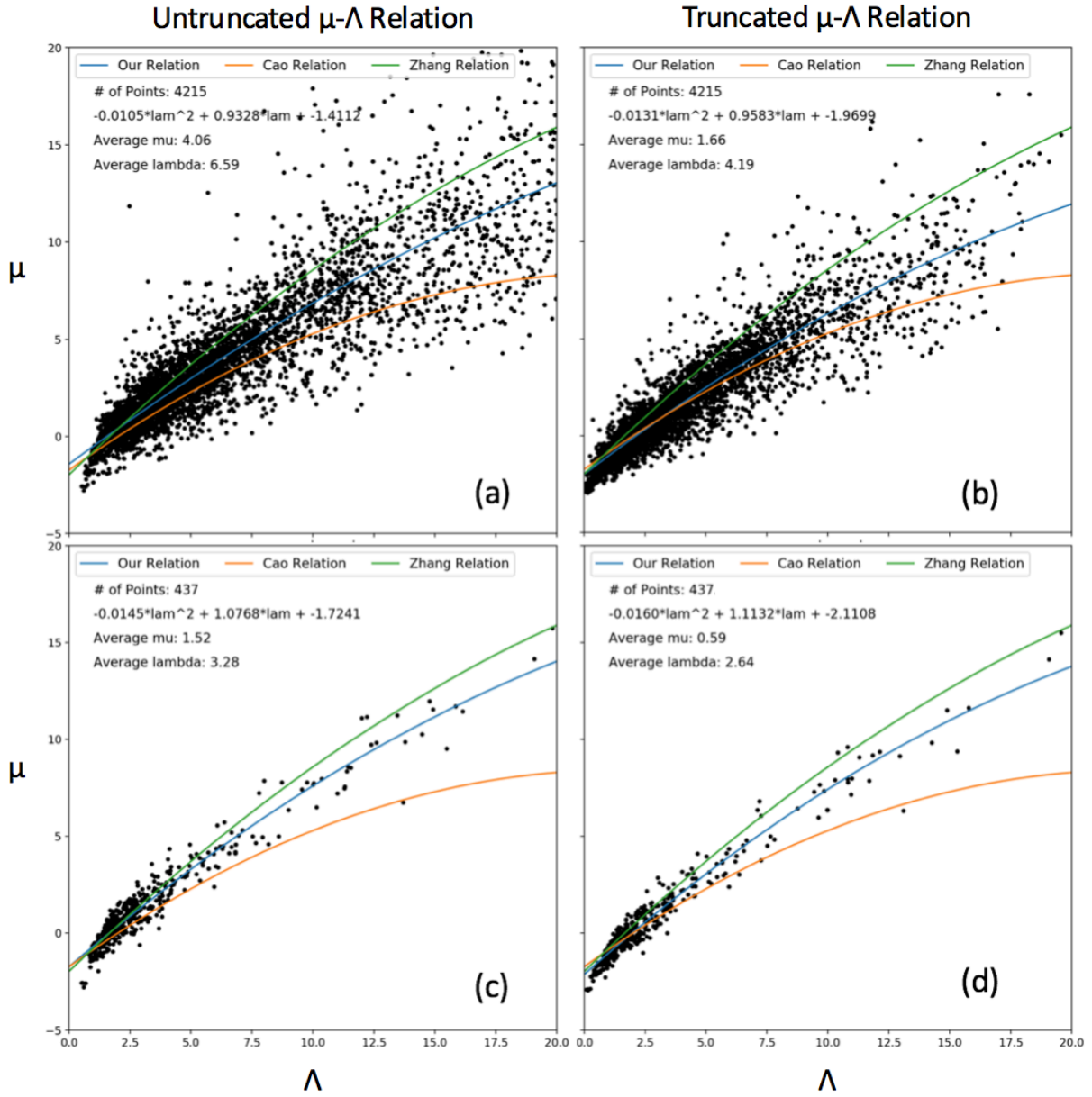
Figure 3. The μ-Λ relations derived from (a) the unfiltered and untruncated data, (b) the unfiltered and truncated data, (c) the filtered and untruncated data, and (d) the filtered and truncated data. The observed μ-Λ pairs are plotted in black with the fitted relation represented by the blue line. The Cao relation (orange) represents cold rain processes and the Zhang relation (green) represents warm rain processes.
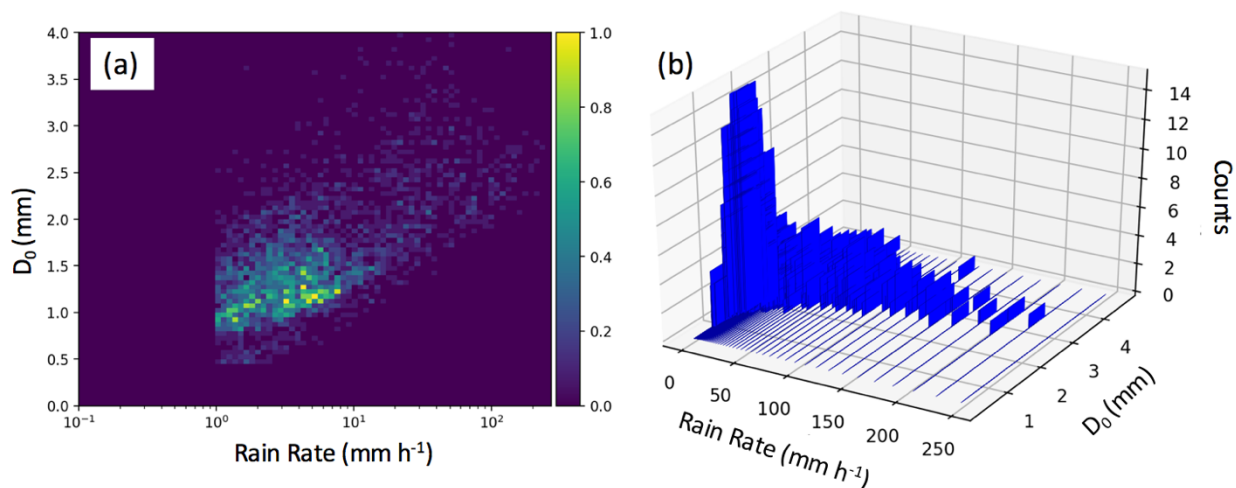
Figure 4. The frequency of DSDs observed in each R (mm h^{-1}) -D_0 (mm) grid box after performing the SATP method on the unfiltered data set. A two-dimensional view is provided in (a) while a three-dimensional view is provided in (b).

To further improve the μ-Λ relation, the SATP method is used to average similar DSDs together, in order to reduce the effects of sampling errors on the μ-Λ relation. The entire unfiltered data set is utilized for the SATP method. Figure 4a gives a two-dimensional view of the sorting of the DSDs, while Figure 4b provides a three-dimensional view. From these figures, it is clear that most of the DSDs within the data set are observed at rain rates of less than 10 mm h^{-1} and have median volume diameters of between 0.5 and 1.5 mm. As one would expect, increases in rain rate coincide with increases in median volume diameter, as broader distributions with longer tails are often observed with higher rain rates. To validate the use of binning and averaging DSDs with similar physical properties, example DSDs are shown in Figure 5. In both examples, each of the observed DSDs in the bin (gray lines) are well represented by the averaged DSD (black line). This result suggests that by using two parameters to sort and average DSDs, the overall shape and slope of the observations are preserved, thereby also preserving the underlying physical properties associated with the DSDs.
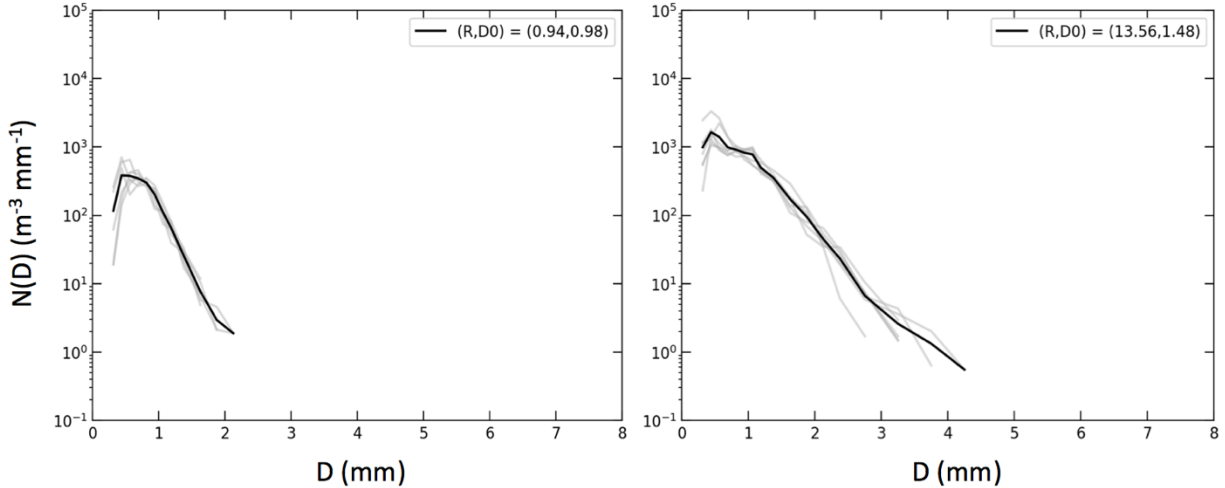
Figure 5. Example DSDs from the SATP method, with the light gray lines representing the observed DSDs from the R-D_0 grid box and the black line representing the new, averaged DSD for the grid. The median R and D_0 of the grid box are displayed in the top right corner.

Once the group of averaged DSDs is calculated, they are fit with gamma distributions using the method of moments and the truncated moment fit. New μ-Λ relations are then found from both methods. The results are shown in Figure 6. Each method results in about 1100 points, one for each grid box where an averaged DSD is found and is able to be fit with a gamma distribution. The average μ and Λ values for each are comparable to what was found with the $R < 5$ mm h^{-1} and counts < 1000 filter. These new SATP μ-Λ scatterplots also exhibit a relatively low amount of spread, with most of the points concentrated towards lower μ and Λ values. The biggest difference observed when using the SATP method is that the overall slope of the relation is lower than what is observed in the Figure 3 relations, with the SATP relations following more closely to the Cao relation. Because lower μ values are being produced for the same values of Λ, this implies that southeastern DSDs are broader than the maritime Florida DSDs. Overall, all of the μ-Λ relations displayed in Figures 3 and 6 produce similar results, with the southeastern relation lying between the Florida and Oklahoma relations.
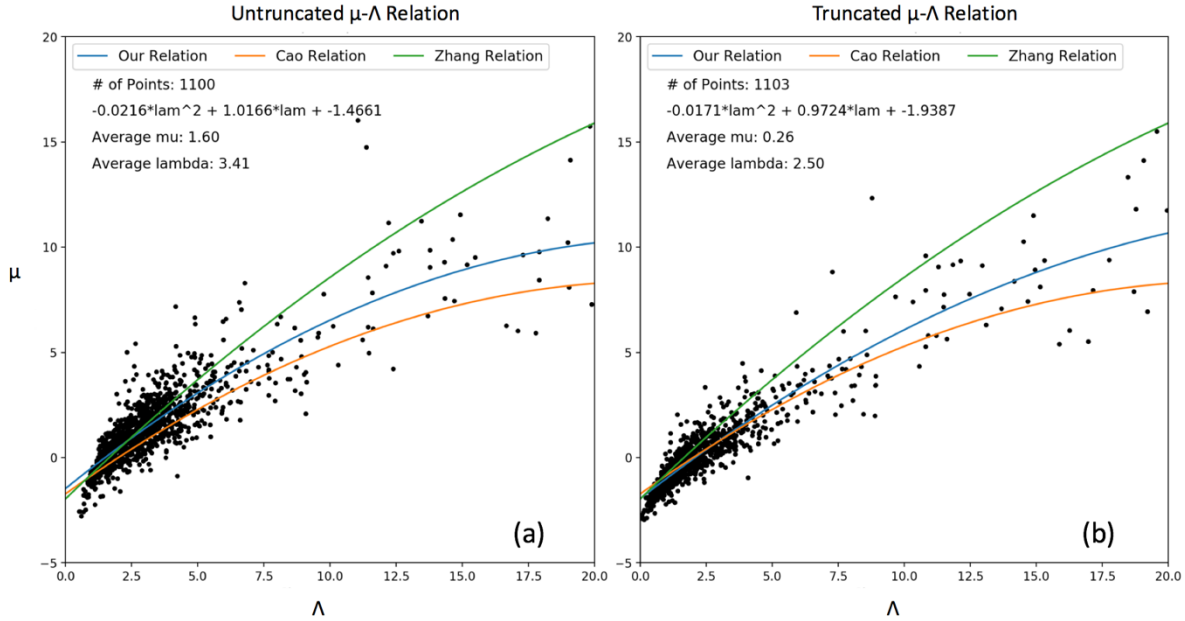
Figure 6. The same as Figure 3, but with the μ-Λ relations produced from the SATP method where (a) represents the untruncated results and (b) represents the truncated results.

The σ_m-D_m relation is used to validate the μ-Λ relation by comparing the retrieved σ_m and D_m values to the disdrometer observations. Both σ_m and D_m are calculated directly from DSD observations, remaining unaffected by sorting and fitting procedures performed on the data (Cao et al. 2008). In Figure 7, the observed σ_m and D_m values are plotted in black, with the retrieved values overlaid in blue. The retrieved σ_m-D_m relation closely matches the observations, especially for $\sigma_m < 2$ mm, suggesting that the μ-Λ relation is valid and represents rain physics (Zhang et al. 2003). Beyond this point, the retrieval relation seems to be slightly overestimating spectrum width and there is larger scatter in the observations, as these points are likely from DSDs with long tails (Cao et al. 2008). Table 2 displays the σ_m and D_m results from the disdrometer-based retrieval. Comparing the bias and correlation coefficients between our results and those obtained by Cao et al. (2008), the results are consistent between the two data sets and it is seen that the retrieval results agree well with the observations, further validating the μ-Λ relation.

Table 2. Disdrometer-based retrieval results for σ_m-D_m from VORTEX-SE and Cao data sets.

	Our D_m	Cao D_m	Our σ_m	Cao σ_m
Bias (%)	-5.53	-2.18	2.74	-1.15
Corr. Coeff.	0.929	0.915	0.991	0.985
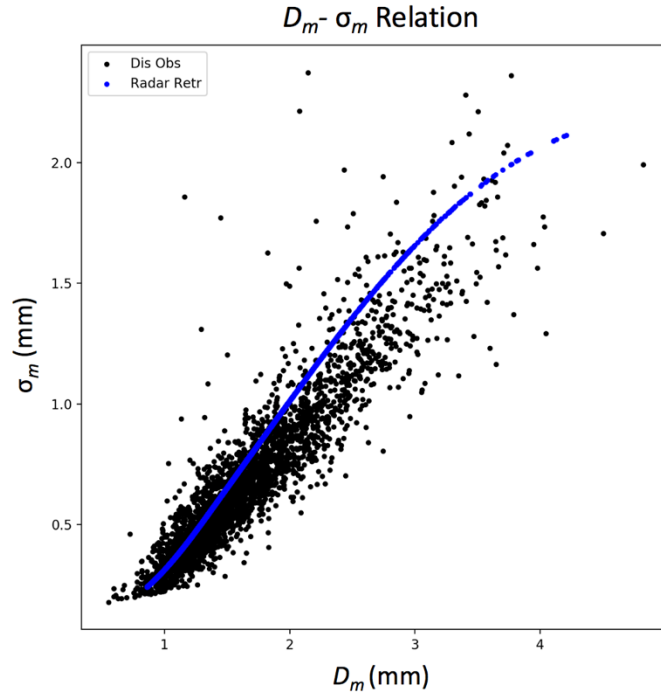
Figure 7. A scatterplot of D_m versus σ_m, where the observed values are the black dots and the radar retrieved values are the blue dots.

ii. Retrieved Rain Parameters

With the μ-Λ relation derived from the SATP truncated moment fit method (Fig. 6b), radar retrievals can be performed with the entire data set. The four main rain parameters focused on in this analysis are rain rate, water content, total number concentration, and median volume diameter (R, W, N_T, and D_0). Figure 8 contains scatterplots of all four variables, comparing the radar retrieved parameters with the disdrometer observed parameters. Each of the scatterplots is color-coded by rain rate, to examine at which rain rates the retrievals perform the worst. All four scatterplots exhibit a wide amount of scatter, with the points that deviate the most from the one-to-one line occurring at the lower rain rates. At low rain rates, measurements can be unreliable due to the smaller samples and the corresponding DSDs are not represented well by a gamma fit. Because of this, measurements with $R < 1$ mm h^{-1} and counts < 50 min^{-1} are filtered out for the remainder of the analysis. The gap in data points in each plot is due to the use of empirical relations for $Z_{DR} < 0.1$ dB. Creating empirical relations based on the VORTEX-SE data set would likely reduce or eliminate this artifact.
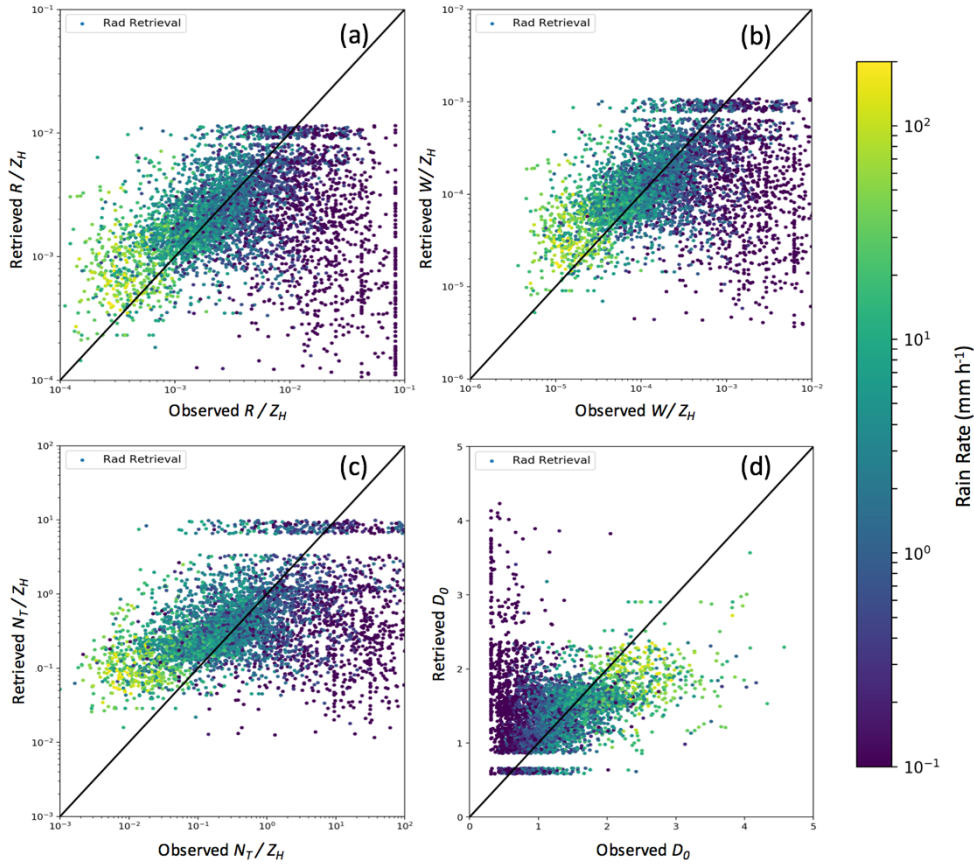
Figure 8. Disdrometer observed rain parameters versus radar retrieved parameters for the entire data set: (a) R/Z_H, (b) W/Z_H, (c) N_T/Z_H, and (d) D_0. The points are sorted by observed rain rate.

Figure 9 contains the radar retrieval results with the new filter applied ($R < 1$ mm h^{-1}, counts < 50 min^{-1}). With 2941 1-min DSDs remaining, the scatter is reduced, suggesting the retrieval performs better for moderate rainfall. During moderate rainfall, the DSD is likely to be broad and follow a gamma distribution more closely, resulting in better retrieval results. The further the observed DSD deviates from a gamma distribution, the worse the retrieval results will be. Table 3 displays the disdrometer based retrieval results for the four rain parameters using this filtered data set, and compares the results to what was found by Cao et al. (2008). Overall, similar performance is seen between the two, and good agreement is seen between the disdrometer-based retrievals and the observations. R, W, and N_T all show positive biases, with N_T exhibiting the worst bias. This result suggests that the radar retrieval is overestimating N_T relative to the disdrometer. With the disdrometer not observing drops in the lowest two diameter bins, it is reasonable to suspect that this would lead to the underestimations in the observed N_T.
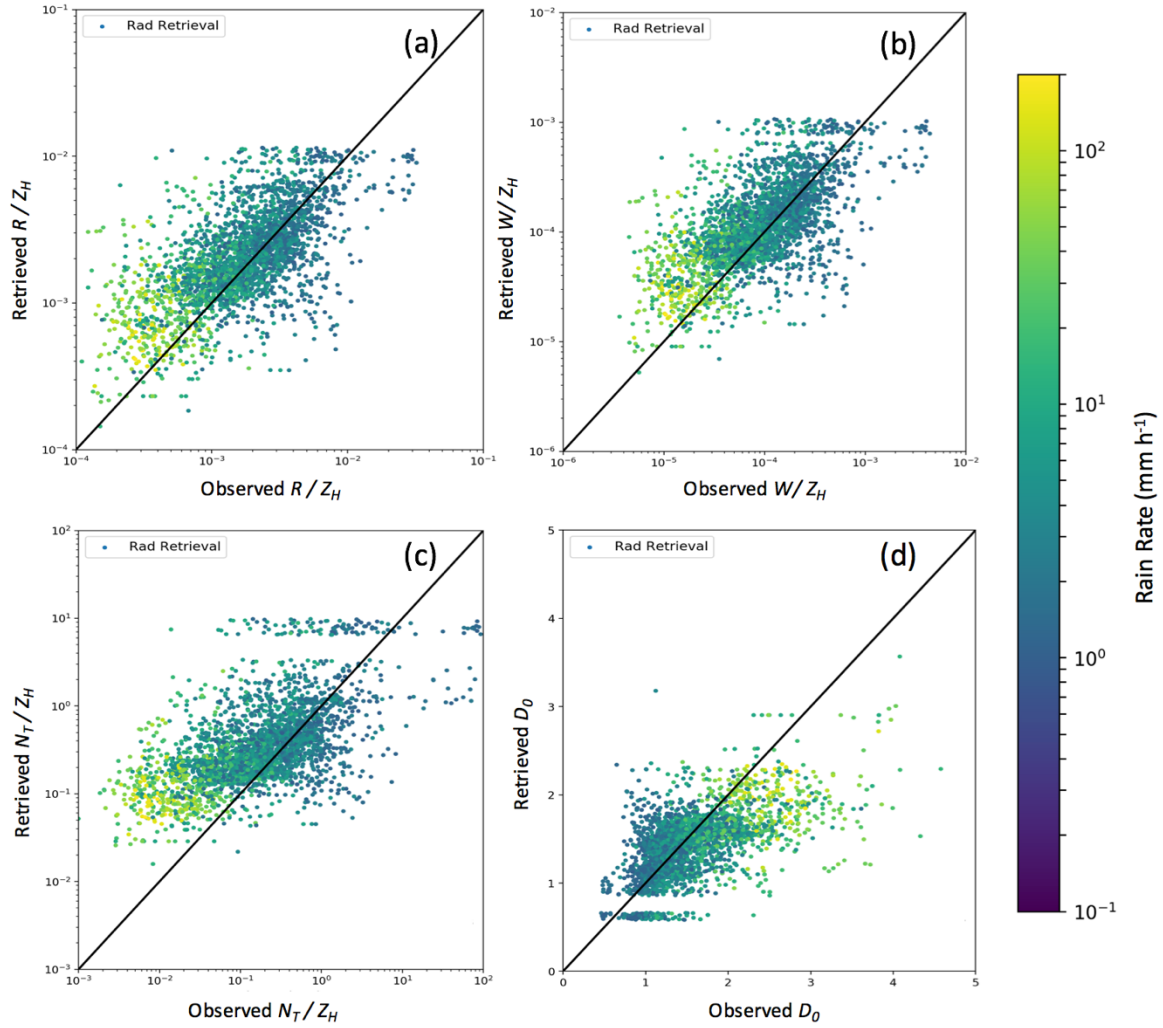
Figure 9. The same as Figure 8, but now with data points where $R < 1$ mm h^{-1} and counts < 50 filtered out.

Table 3. Disdrometer-based retrieval results for the VORTEX-SE and Cao data sets for the four physical parameters $R, W, N_T,$ and D_0.

	Our R	Cao R	Our W	Cao W	Our N_T	Cao N_T	Our D_0	Cao D_0
Bias (%)	5.41	3.37	10.18	2.52	110.46	14.16	-0.71	8.73
Corr. Coeff.	0.984	0.986	0.970	0.967	0.713	0.763	0.867	0.819

b.   Case Studies

i.   IOP 4B – 2016

On April 29, 2016, a strong QLCS with a large region of trailing stratiform rain passed through the VORTEX-SE domain in western Alabama. The position of the PIPS relative to the approaching QLCS is provided in Figure 10a. The storm passed over the PIPS from 2124-2357 UTC. Strong circulation was observed within the QLCS in Mississippi, but the circulation weakened upon approaching the PIPS. The closest WSR-88D radar was the Columbus AFB, MS KGWX, which was 63.8 km away and scanned 0.80 km above the PIPS. In Figure 10b, time series of the relative humidity, dew point and temperature, and wind speed and wind direction are shown. At 2158 UTC, there was an increase in relative humidity to about 95% and a 5° decrease in temperature, indicating the passage of a gust front shortly before the leading edge of the storm reached the PIPS. The strong convective region of the QLCS passed over the disdrometer until 2218 UTC, and then the precipitation transitioned into stratiform rain, which remained over the disdrometers until they were picked up at 2357 UTC.
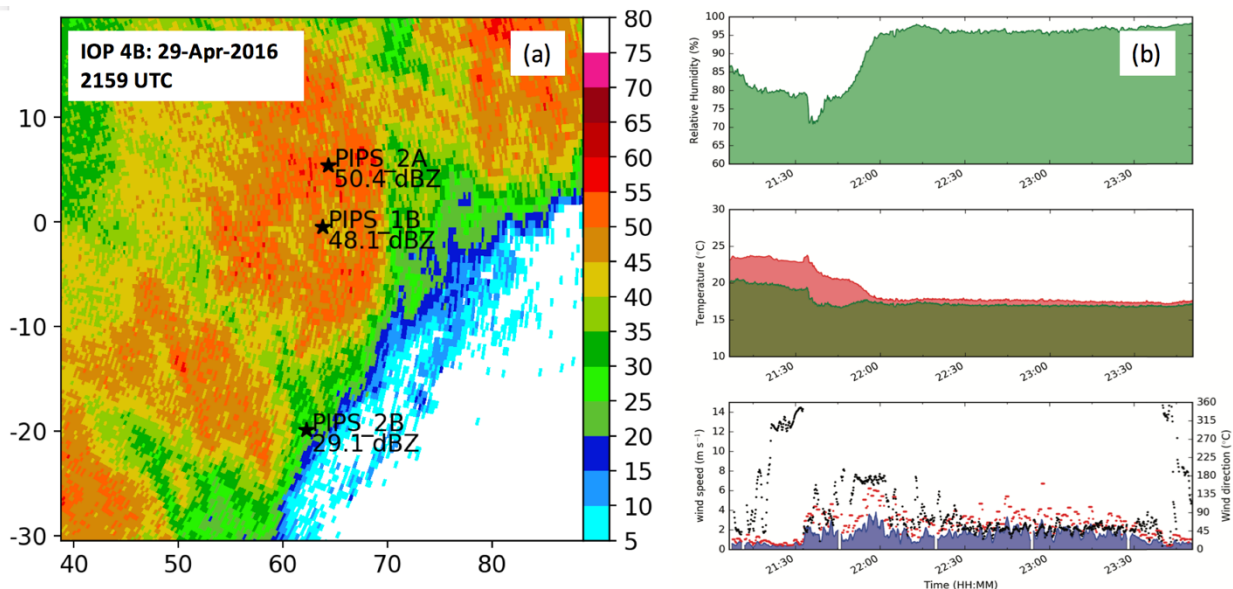
Figure 10. An overview of IOP 4B is presented. (a) Radar PPI plot of KGWX reflectivity (dBZ) as the leading edge of the storm began to pass over the PIPS. The PIPS locations are overlaid, with the KGWX observed reflectivity at each instrument. (b) Time series of relative humidity (%, top), temperature and dew point (°C, middle), and wind speed (m s^{-1}, red dots) and wind direction (black dots, bottom) from PIPS 2B.

A comparison of observed DSDs in the leading edge of the QLCS versus in the reflectivity core of the storm over PIPS 2B is presented in Figure 11. In the leading edge (Fig. 11a), the observed DSD is poorly fit by a gamma distribution, as there are more large drops and fewer small drops than a gamma distribution fit would expect. It is observed that none of the distributions used fit this type of DSD well, as the TMF and retrieval fits are also underestimating the number of small drops. The radar observed Z and disdrometer calculated Z values are very different, with the disdrometer seeing a reflectivity that is 9 dBZ higher than the radar observations. Due to the unusual shape of the leading edge DSD and the large difference in radar and disdrometer Z values, the radar retrieved D_0 value is 1 mm smaller than what the disdrometer observed. In the reflectivity core (Fig. 11b), the observed DSD follows a gamma distribution much more closely than in the leading edge of the storm. This results in the various fitting procedures fitting the observed DSD more closely. The radar retrieved fit is underestimating the overall DSD, but still results in a D_0 value within 0.05 mm of the disdrometer observation. It is most likely that the radar retrieved DSD is consistently underestimated due to the lower Z that the radar is seeing at this time, as compared to the disdrometer.
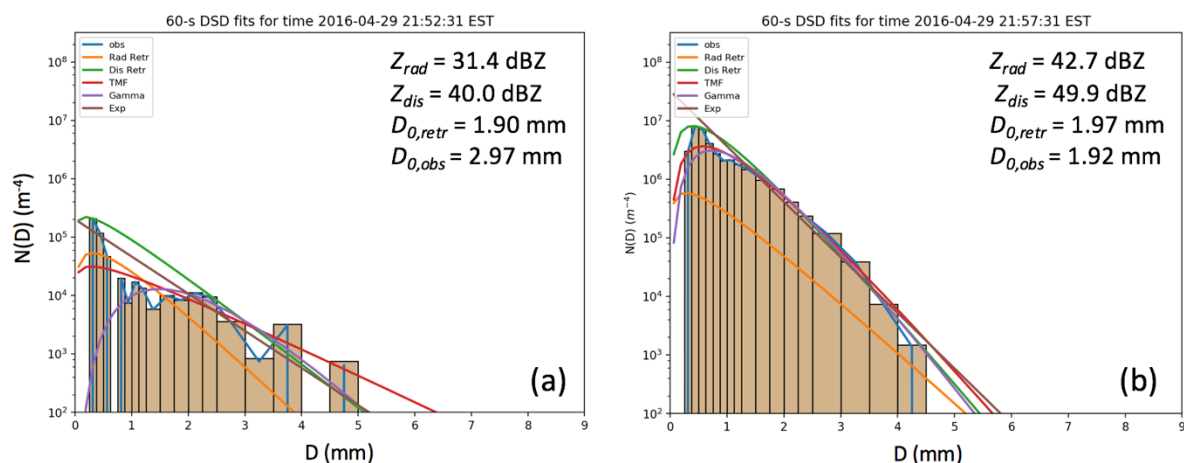
Figure 11. Plots of observed DSDs from PIPS 2B in the leading edge (a) and reflectivity core (b) of the QLCS. Overlaid are the radar retrieved (orange), disdrometer retrieved (green), TMF (red), gamma (purple), and exponential (brown) fits.

Time series of reflectivity *Z* and differential reflectivity Z_{DR} over PIPS 2A are presented in Figure 12. Plotted underneath each polarimetric variable is the time series of the 1-min number concentrations observed by PIPS 2A. Maximum reflectivity (50 dBZ) and differential reflectivity (2 dB) were observed at 2201UTC, as the strongest convection passed over the disdrometer. The broadest DSDs were also observed during this period of strong convection. *Z* and Z_{DR} then decreased, and during the transition period from 2225-2250 UTC, *Z* remained below 30 dBZ while Z_{DR} remained below 0.5 dB. Both variables then increased slightly as the stratiform rain passed over. Throughout the entire time period, the disdrometer consistently reported larger *Z* and Z_{DR} values than the radar, especially for Z_{DR} during the stratiform rain. A lot of the differences observed could be due to the time scale differences, with the disdrometer values being derived every minute, while the radar scanned over the disdrometer every 5-8 minutes, failing to capture much of the temporal variability that the disdrometer observed. It is possible that there is also a systematic bias in either the radar or disdrometer measurements that is not currently being taken into account.
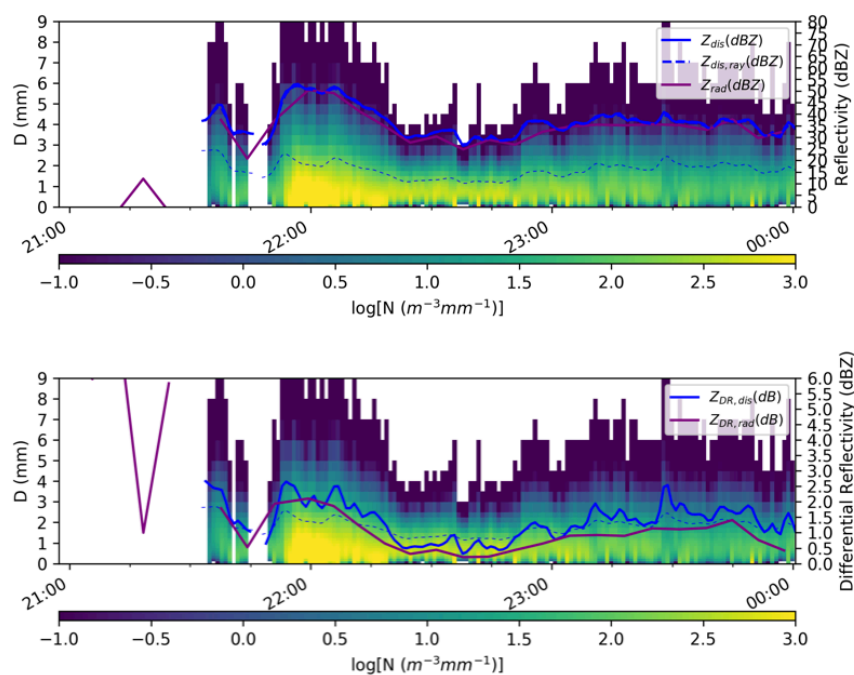
Figure 12. Time series of reflectivity (top) and differential reflectivity (bottom) over PIPS 2A during IOP 4B. The polarimetric variables estimated by PIPS 2A are plotted in blue, while the radar observed variables are plotted in purple. The blue dashed line is the disdrometer measured median volume diameter. Plotted underneath the polarimetric variables are the 1-min number concentrations from the TMF fit to the disdrometer observations.
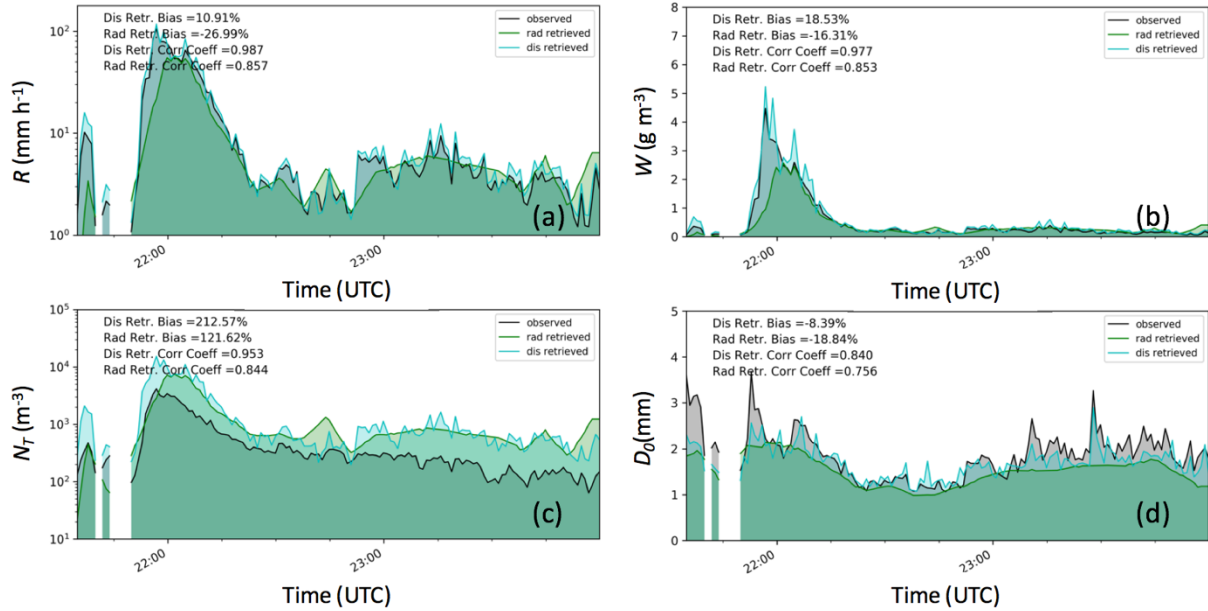
Figure 13. Time series of (a) rain rate, (b) water content, (c) total number concentration, and (d) median volume diameter over PIPS 2A during IOP 4B in 2016. Each time series compares the disdrometer observations (black) with the disdrometer Z, Z_{DR} retrieval (blue) and radar Z, Z_{DR} retrieval (green).

Time series of the four rain parameters are shown in Figure 13, with the observation plotted in black, the disdrometer retrieval in blue, and the radar retrieval in green. Peak values of all four rain parameters were observed as the QLCS leading edge passed over PIPS 2A. W, R, and N_T values decreased after the main convection passed, while D_0 reached similar values during both the convective and stratiform rain periods. This shows that similar magnitudes of D_0 can be observed in very different rain rates, exemplifying the importance of using two parameters to sort similar DSDs, rather than one. The radar retrieval consistently overestimates N_T and underestimates D_0. It also struggles to reproduce the peaks in R and W observed by the disdrometer. Overall though, very good agreement is observed between the retrieved and the observed values.

The radar retrieval method can be used to derive rain parameters across an entire storm. In Figures 14-16, radar PPI (plan position indicator) of some of the retrieved parameters are pictured for three locations in the storm. Figure 14 displays the results across the storm at 2159 UTC as the leading edge passed, and the radar was dominated by convective precipitation. Figure 15 displays the storm 32 minutes later at 2231 UTC, as the transition zone moved through the area. Finally, Figure 16 displays the storm at 2238 UTC, as the large region of stratiform rain began to move out

of the domain. The top left and right panels for Figures 14-16 plot the radar observed Z and Z_{DR} respectively. The middle-left panel pictures the retrieved R while the middle-right panel shows the retrieved D_0. Finally, the bottom row displays the radar-retrieved μ and Λ values, which represent the overall shape and slope of each underlying DSD.

In Figure 14, multiple reflectivity cores with maximum Z above 45 dBZ are observed, each corresponding with pockets of $Z_{DR} > 1.5$ dB, indicating larger drops. Looking at the rain rate PPI, the areas of highest rain rate correspond with the reflectivity cores, and there is a sharp increase in rain rate from the front edge to the reflectivity cores. As expected, in these areas of local maxima, D_0 also experiences a slight increase, owing to the presence of a larger range of drop diameters being observed in this area. Finally, local minimums of μ and Λ values are observed in the reflectivity cores, as these high rain rate DSDs are broad and gentle in slope. At the very front edge of the storm, an area of very low Z and high Z_{DR} is observed. This is likely the "big drop" region of the storm, where sparse amounts of large drops fell ahead of the reflectivity core. As discussed in Cao et al. (2008), the radar retrieval tends to perform poorly in this region of the storm, as the retrieval method "expects" these Z and Z_{DR} values to correspond with large numbers of small drops instead of small numbers of large drops. Because of this, the retrieval is calculating lower values of D_0 and larger values of μ and Λ, as it fits a tall and narrow distribution centered at the lowest rain diameters.

In the transition region between convective and stratiform rain shown in Figure 15, there is a large decrease in reflectivity, with most Z values between 15-30 dBZ, and very low Z_{DR} values of below 0.5 dB are observed. These low Z and Z_{DR} values result in patchy radar retrievals, as the retrieval struggles to fit distributions at low Z_{DR} values, due to their irregular shape. R remains below 5 mm h^{-1} throughout the region and and D_0 values remain below 1.5 mm. Very high μ and Λ values are found throughout this region, with both parameters frequently reaching above 15, corresponding with very narrow distributions dominated by small drops.

The end portion of the large trailing stratiform region is shown in Figure 16. The area exhibits reflectivity values that are in-between what was observed in the convective and transition regions, with Z values ranging mainly between 30 and 40 dBZ. Z_{DR} values range between 0.5 and 1.5 dB, about 1 dB lower than what is observed in the regions of strong convection. Rain rate remains very low in this region ($R < 5$ mm h^{-1}), as in the transition region. D_0 values range from between 1.5 and 2 mm, comparable to D_0 values that would be found in areas of weaker convection

with higher rain rates. Low µ and Λ values, similar to those found in the convective precipitation, are seen throughout the stratiform region, indicating broad distributions. The broad distributions observed with the lower rain rates suggests that this area contains low concentrations of large drops combined with concentrations of small drops that are lower than what is observed in the convective region. This result is consistent with earlier studies such as Tokay and Short (1996), Waldvogel (1974) and Bringi et al. (2003).
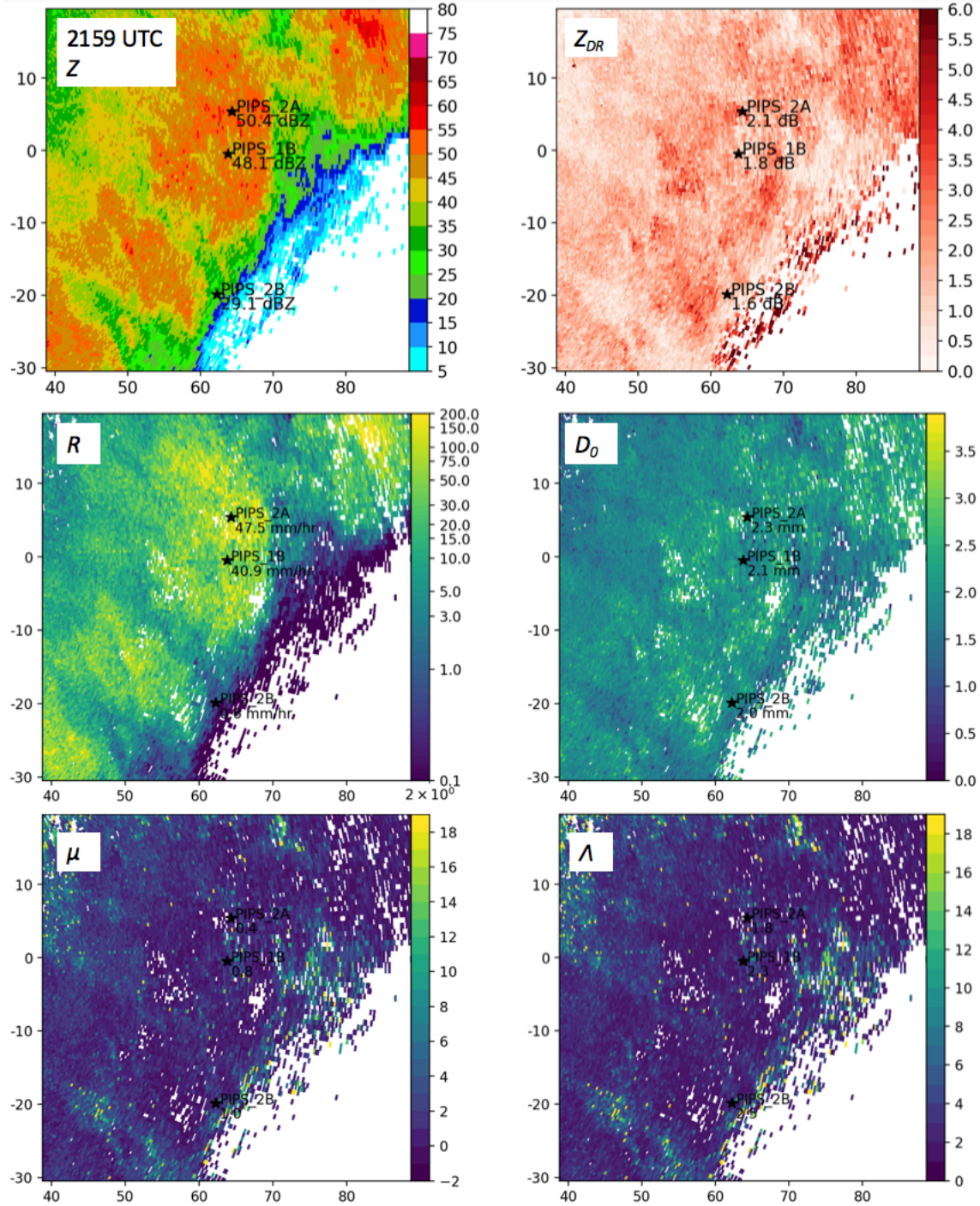
Figure 14. Radar PPI plots from 2159 UTC on 29-Apr-2016 of radar observed reflectivity (Z) and differential reflectivity (Z_{DR}) along with radar retrieved values of rain rate (R), median volume diameter (D_0), DSD shape parameter (μ), and DSD slope parameter (Λ) as the QLCS leading edge passes through the domain.
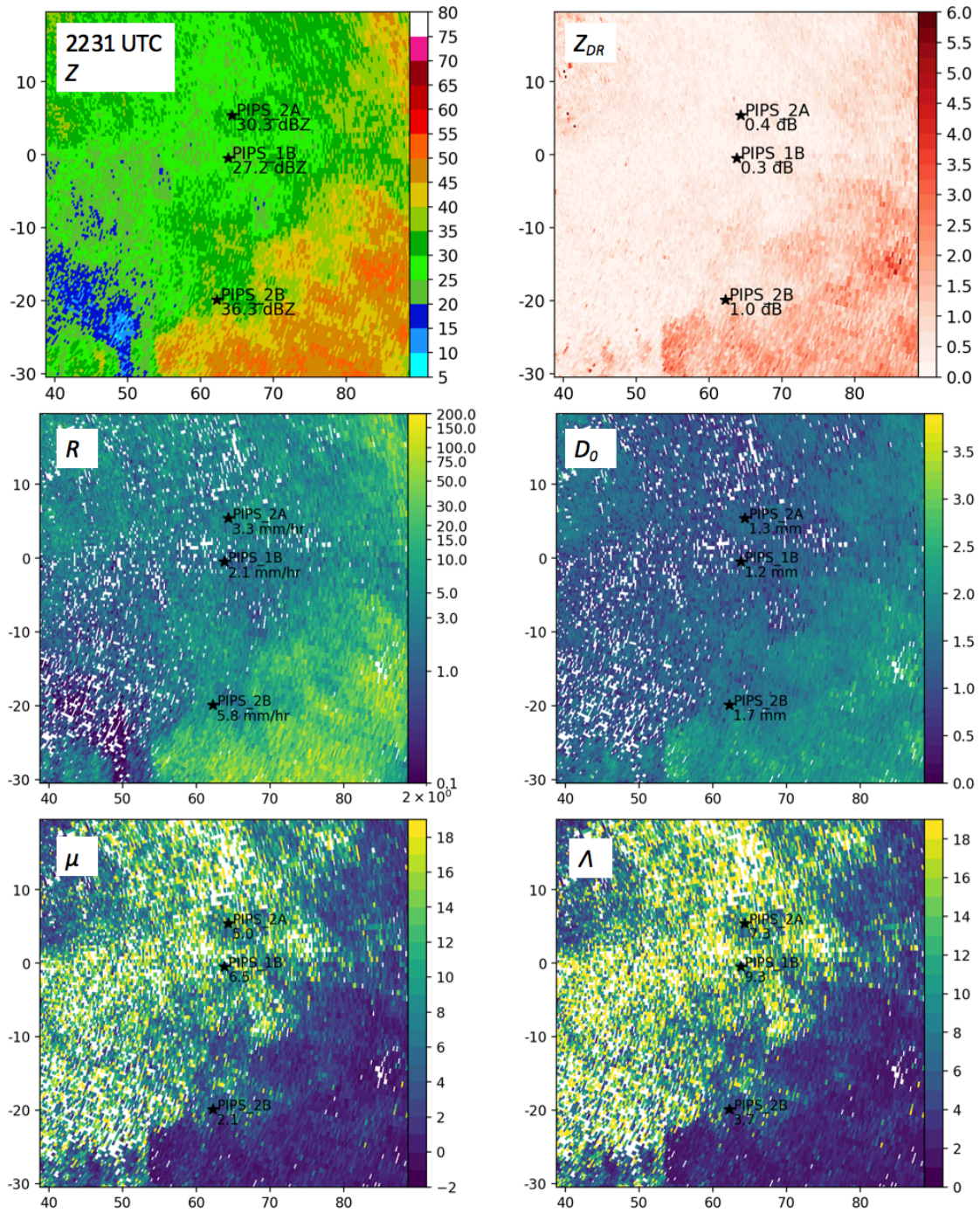
Figure 15. The same as Figure 14, but for 2231 UTC, as the transition between convective and stratiform precipitation occurs.
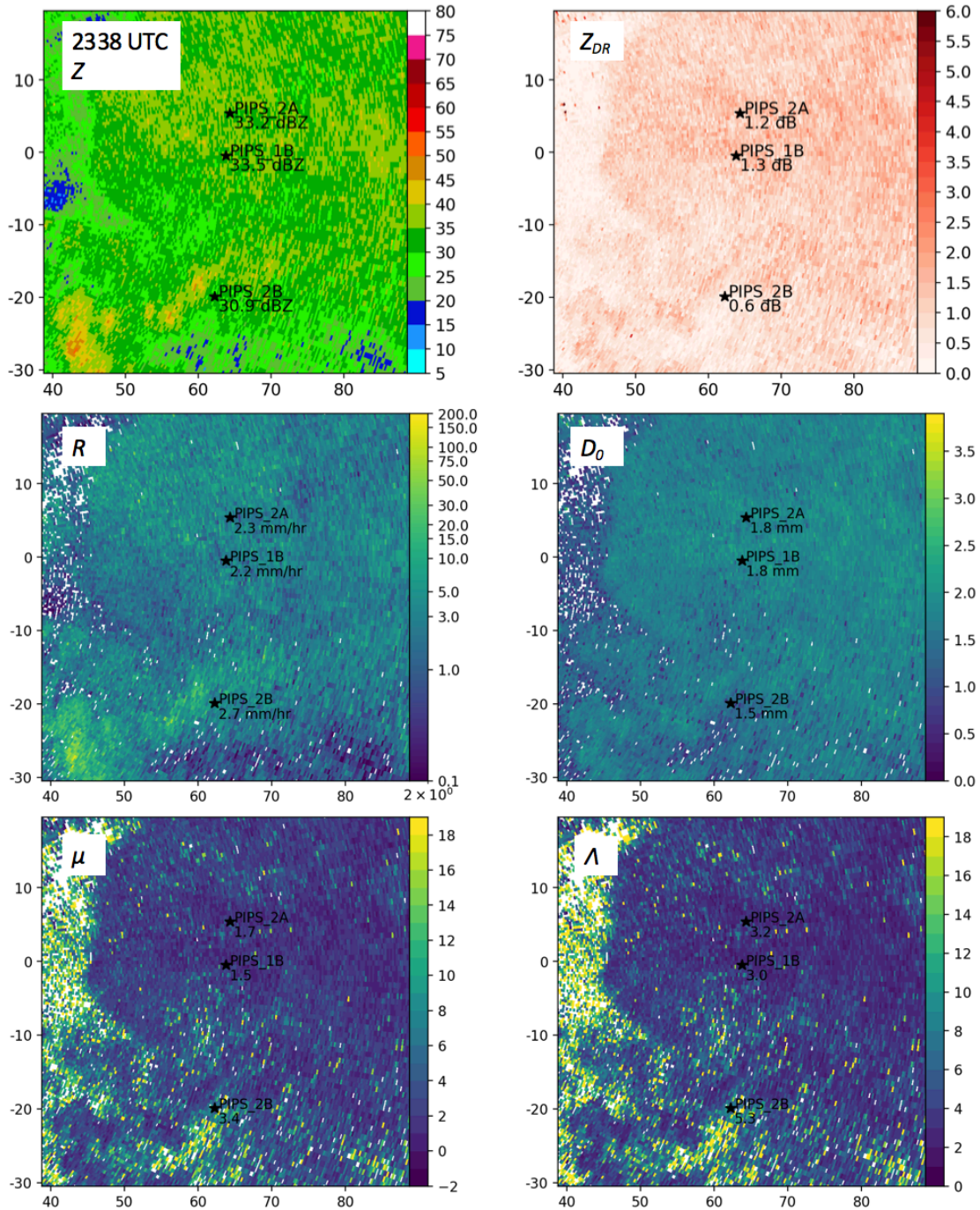
Figure 16. The same as Figure 14, but for 2338 UTC, as the trailing stratiform precipitation covers the entire domain.

ii. IOP 4C – 2016

A supercell cluster passed through the VORTEX-SE domain in north central Alabama on April 30, 2016. The cells exhibited weak rotation as they passed over the PIPS, however, a tornado-warned storm was reported later in association with the supercell cluster. Precipitation passed through the area between 2015 UTC and 2145 UTC; however, the disdrometers were only deployed during part of this period. An example radar PPI of Z is shown in Figure 17, along with time series of relative humidity, temperature, and wind speed and direction. Radar observations for this case were taken from KGWX, which was located 111.9 km away and scanned 1.71 km above the PIPS. The cells began as small, scattered cells, but eventually the cells grew in size, increased in strength, and began to merge around 2041 UTC. As shown in Figure 17b, a brief increase in wind speed was observed around 2120 UTC, as the temperature decreased and relative humidity began to level off at ~95%. Comparing this timing to the time series of Z and Z_{DR} over PIPS 2B in Figure 18, this increase in wind coincides with the passing of the strongest reflectivity core over the disdrometers.
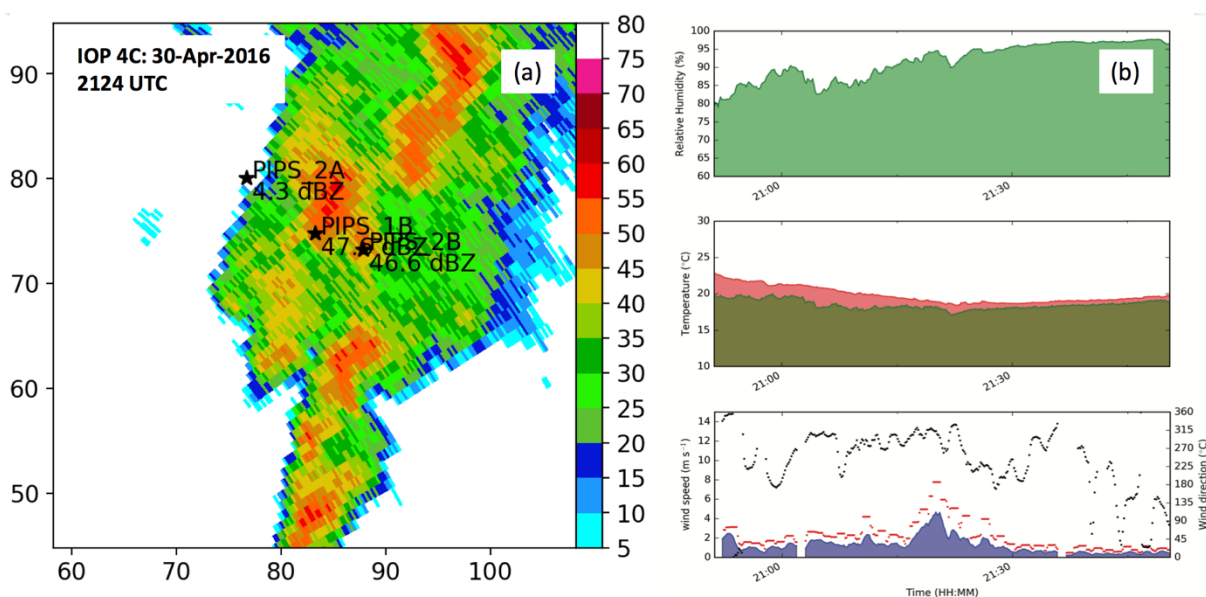
Figure 17. The same as Figure 10, but for IOP 4C-2016 PIPS 2B.
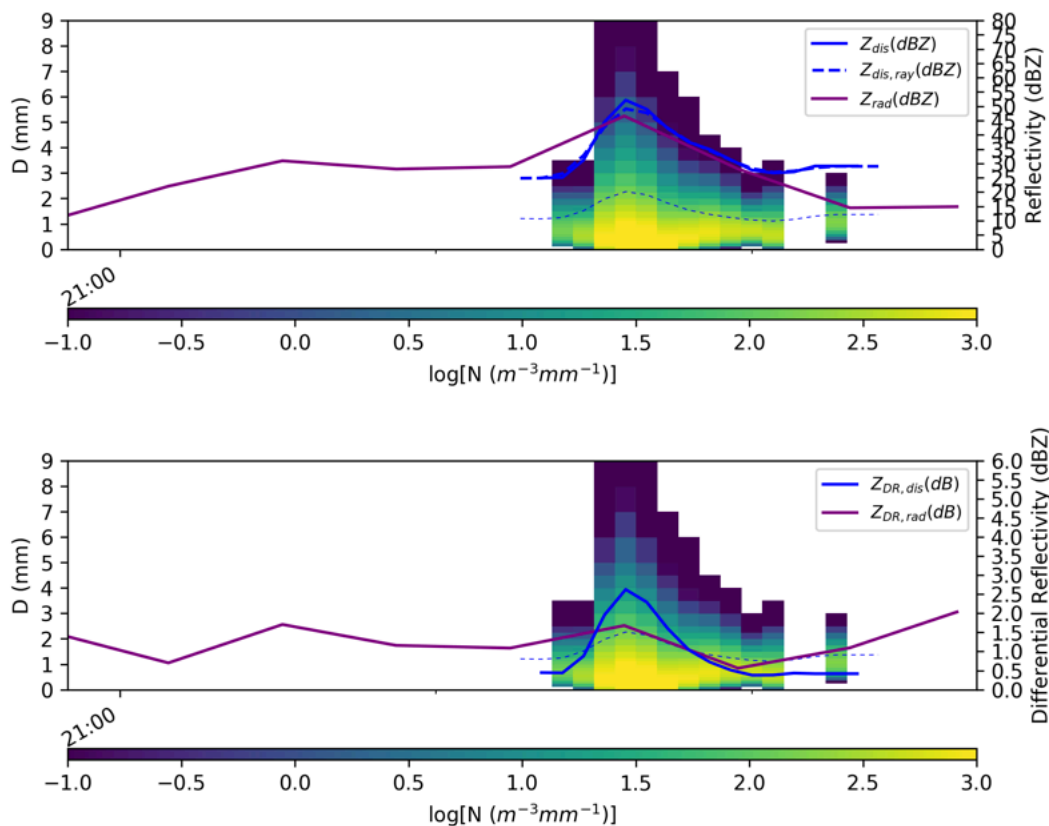
Figure 18. The same as Figure 12, except for PIPS 2B during IOP 4C-2016.

PIPS 2B collected data as the strongest reflectivity core passed through the area, from 2121 UTC to 2131 UTC. The time series in Figure 18 shows that peak Z and Z_{DR} values were observed at 2124 UTC, with Z reaching a maximum of 45 dBZ and Z_{DR} reaching a maximum of 1.5 dB. The maximum D_0 values were also observed at this time, peaking at approximately 2 mm. As observed during IOP 4B, the broadest DSDs occurred with the strongest reflectivities. Overall, it is seen that the disdrometer-estimated Z and Z_{DR} are usually both higher than the radar observed values. The largest disagreements occurred in the disdrometer-estimated Z_{DR} while the reflectivity core passed. A similar trend was found in the IOP 4B data, as mentioned in the previous section. The best agreement between the radar and disdrometer measured polarimetric variables was found after the reflectivity core passed.
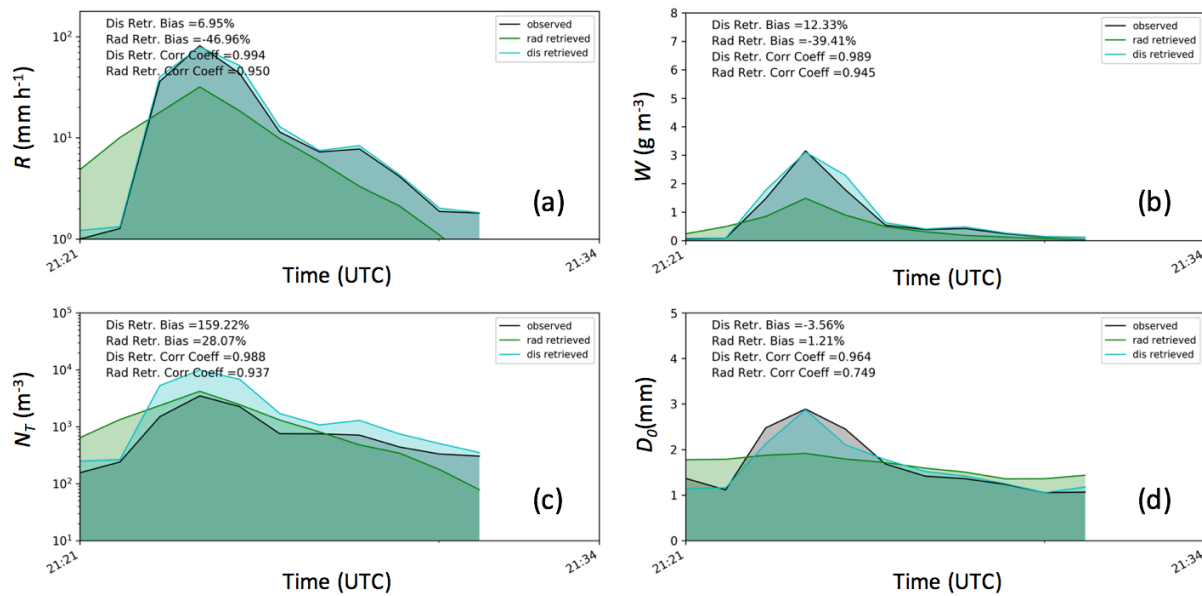
Figure 19. The same as Figure 13, but for PIPS 2B during IOP 4C-2016.

Figure 19 displays time series of the four main rain parameters over PIPS 2B. All four parameters reach maximum values as the reflectivity core passes. The radar-retrieved rain parameters again struggle to match the peak values that the disdrometer is observing. Before the passing of the reflectivity core, the radar retrieved parameters are larger than what the disdrometer was observing. This observation matches the trend of the radar observing larger Z and Z_{DR} than the disdrometer before the core, but the disdrometer then estimating larger Z and Z_{DR} than the radar as the reflectivity core passes. This leads to the implication that the performance of the radar retrievals is dependent on how closely the radar observed and the disdrometer estimated polarimetric variables agree. In large part, the differences between radar and disdrometer measurements can again be related to the differences in observation frequency. The radar is not able to capture the natural variations in the rain physics, while the disdrometer is able to observe the rapid fluctuations occurring in the Z and Z_{DR} fields.
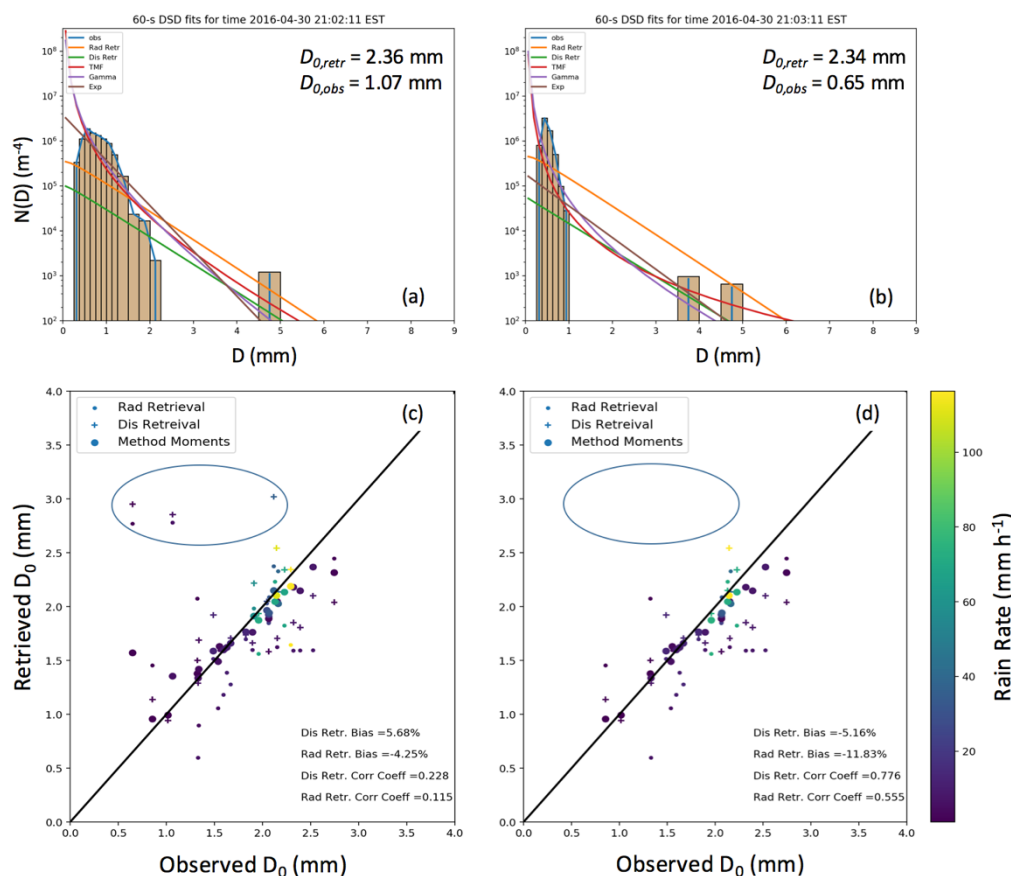
Figure 20. (a) and (b) Two example bimodal DSDs observed by PIPS 1B during IOP 4C-2016. Overlaid are the various fits to the distribution, as in Figure 11. (c) Observed versus retrieved D_0. (d) Same as (c), but with bimodal distributions removed.

Figures 20a and b display two bimodal distributions observed by PIPS 1B in an area of relatively high Z and very high ZDR. Bimodal distributions might arise from overlapping rain shafts in different regions of the storm or at different heights in the same cell (Marshall 1953; McFarquhar et al. 1996; Sauvageot and Koffi 2000) Gamma distributions do not represent bimodal distributions, as gamma distributions assume a continuous distribution. This results in the gamma fits estimating drops in the empty bins between ~2-4 mm. Because of this, the retrieved D_0 is more than double the disdrometer observed value. To remove bimodal distributions, DSDs where a bin is 25% larger than the preceding and proceeding bins for $D>2.25$ mm are removed. Figure 20c shows the D_0 results with bimodal DSDs and Fig. 20d shows results with bimodal DSDs removed. In Fig. 20d, the largest outliers are removed and the correlation coefficients greatly improve. The radar retrieved bias also increases, as the outliers above the line are no longer balancing the underestimated values.

iii. IOP 4C-2017

On April 30, 2017, a mature QLCS with several bowed features entered the VORTEX-SE domain. The PIPS were deployed near an embedded mesocyclone that was tornado-warned. The leading edge of strong convection was followed by a large region of patchy stratiform rain. Precipitation was measured by the disdrometers from 1831-2009 UTC. The nearest radar was KGWX, which was located 120.0 km from the PIPS, and scanned 1.90 km above the instruments. An example PPI plot of reflectivity is presented in Figure 21, along with time series of relative humidity, temperature, and wind speed and direction. At 1831 UTC, the leading edge of the QLCS first began to pass over the PIPS. This passage is reflected in the time series, as there is a very sharp increase in relative humidity and sharp decrease in temperature at this time, as well as a rapid change in wind direction. Around 1847 UTC, the precipitation transitioned to stratiform rain, which continued to pass over the PIPS until they were picked up at 2009 UTC.
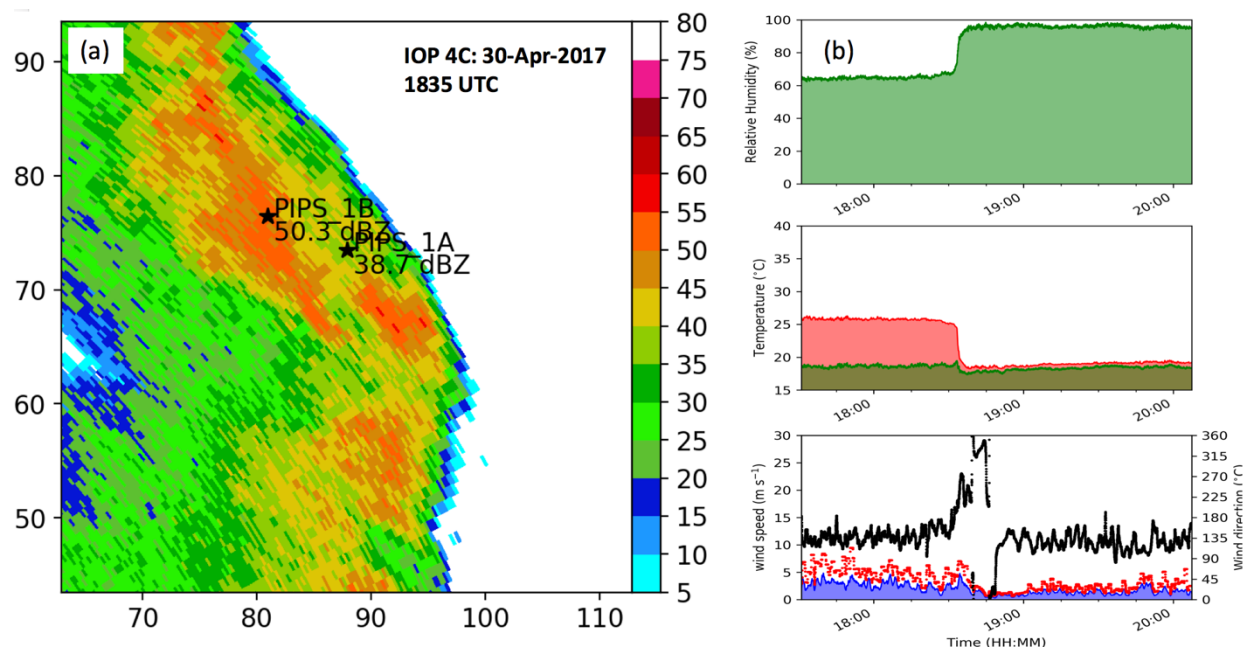
Figure 21. The same as Figure 10, but for PIPS 1B during IOP 4C-2017.

Figure 22 displays the reflectivity, differential reflectivity, and correlation coefficient time series over PIPS 1B. Similar trends from the previous IOPs are also found in these time series. Reflectivity quickly reaches a maximum value of 50 dBZ, and Z_{DR} reaches a maximum of 1.5 dB, as the leading edge passes over PIPS 1B. During the transition period, the data are masked out due to the low rain rates observed in portions of the patchy stratiform rain. In the stratiform rain, lower N_T are observed at all diameters, but D_0 reached values similar to those observed during the convective rain. Similar to the two other case studies analyzed, the disdrometer-estimated Z and Z_{DR} are consistently higher than the values observed by the radar. In this particular storm, the disdrometer-estimated Z_{DR} is almost twice as large as what the radar is observing across the entire time series. It is expected that this will result in larger disagreements between the radar retrieved parameters and disdrometer observed values for this case.
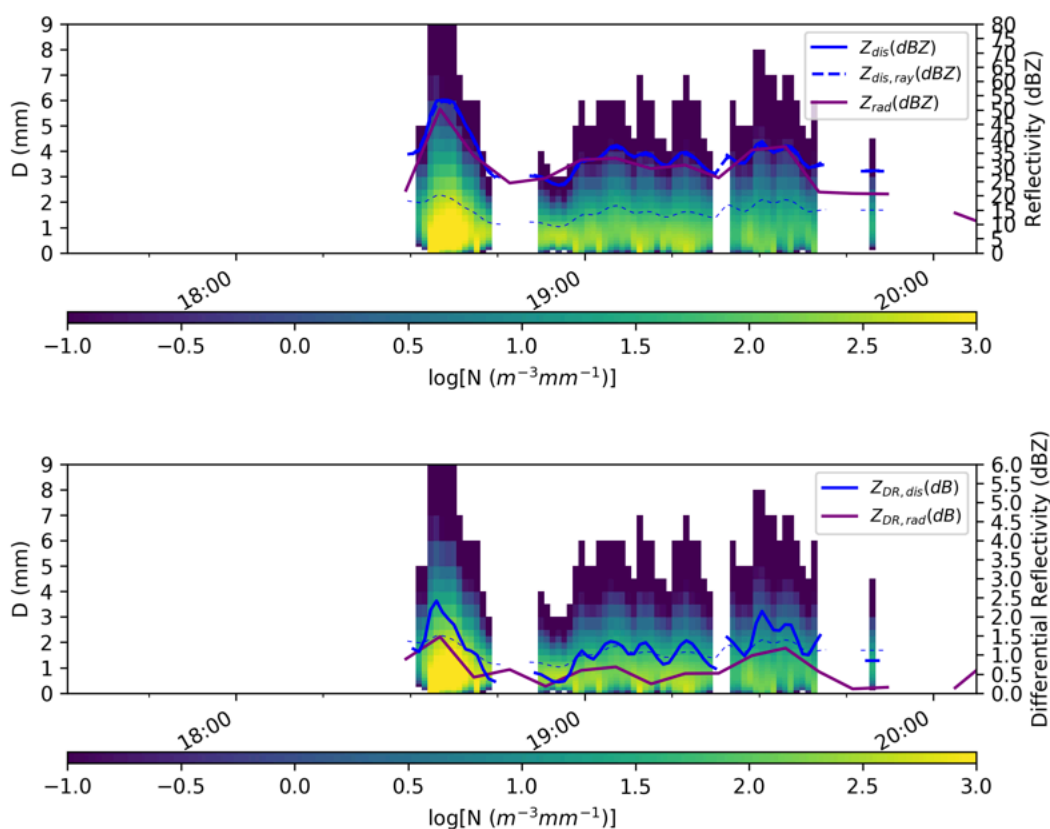
Figure 22. The same as Figure 12, but for PIPS 1B during IOP 4C-2017.

Figure 23 displays the time series of R, W, N_T, and D_0 for PIPS 1B. Besides D_0, all parameters reach their maximum values during the convective rain. As mentioned earlier, D_0 reaches similar ranges of values in both the convective and stratiform rain. The radar retrieved R, W, and D_0 continue to be lower than what the disdrometer observes during periods of strong convection. However, the supercell analysis (IOP 4C-2016) showed a greater tendency for the radar retrieved parameters to be lower than the disdrometer observations in convective precipitation. In stratiform rain, the radar retrieved values of N_T, R, and W are larger than what the disdrometer is observing, which is similar to what the stratiform region of IOP 4B showed, although in IOP 4B the overestimations do not appear to be as large as the discrepancies observed in this case.

As all three cases showed disdrometer estimated Z and Z_{DR} to be consistently higher than what the radar observed, it is necessary to look for other possibilities to explain why sometimes the radar retrieval results in a majority of under or overestimated rain parameters. When looking at all three cases, it is seen that underestimations of radar retrieved R, W, and N_T values tend to occur during periods of convective rain, while overestimations tend to occur during stratiform rain. This might signify a need to create different μ-Λ relations or a slightly different retrieval method based on the precipitation mode.

Figure 23. Same as Figure 13, but for PIPS 1B during IOP 4C–2017.

6. CONCLUSION

In this study, disdrometer data from the 2016 and 2017 VORTEX-SE field programs were analyzed and compared with nearby radar observations. Retrievals of DSD parameters from polarimetric radar measurements were performed using the constrained-gamma retrieval method. In order to perform the 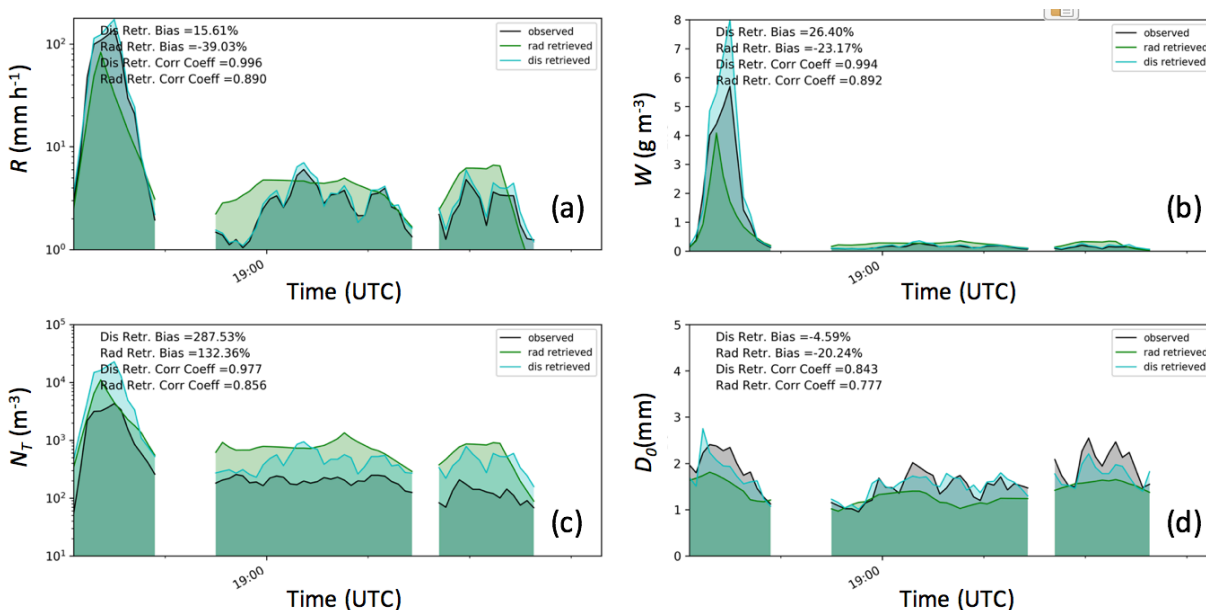radar retrievals, the VORTEX-SE disdrometer observations were used to derive a new μ-Λ relation that is specific to the southeastern United States climatology. The new relation is compared to previous relations found by Zhang et al. (2001) and Cao et al. (2008). These existing relations were derived from rainfall measurements in Florida and Oklahoma, which both represent different climatic regimes. Even when using different processing and filtering techniques, the Southeast U.S. μ-Λ relation consistently fell between the Florida and Oklahoma relations, suggesting that storms in the Southeast U.S. occur in environments that are influenced by both the continental, cold rain processes (as in the Great Plains) and maritime, warm rain processes (as in Florida).

The final μ-Λ relation was derived using the SATP method, which sorts DSDs into bins that represent DSDs of similar physical properties. Two parameters were used to sort the DSDs: rain rate and median volume diameter. These parameters were chosen because they are derived from the middle moments of the DSD, which are the moments that are most accurately estimated. By averaging similar DSDs together, the effects of sampling errors are assumed to be reduced. The truncated moment fit was then used to fit the averaged DSDs with gamma distributions. The truncated moment fit resulted in better-fitting gamma distributions, as the method is predicated on the assumption that DSDs are observed within a finite range, rather than an infinite range. The μ-Λ relation was then derived from the averaged DSD of each bin, which helped prevent the relation from being dominated by low rain rate DSDs.

The retrieval method was then performed with this μ-Λ relation. Disdrometer-measured Z and Z_{DR} were used to perform initial retrievals in order to validate the methods and accuracy of the retrieval method. The disdrometer observations and disdrometer based retrievals of rain parameters showed very good agreement, validating the utility of the retrieval method. The μ-Λ relation was then used to perform radar retrievals for the entire VORTEX-SE data set. The results showed a large amount of scatter, with the largest outliers occurring at lower rain rates. This suggests that retrieval methods do not perform as well at lower rain rates, likely because sampling

errors are higher and these DSD shapes can differ greatly from the shape of the gamma distribution. As rain rate increases, the DSD becomes broader, better matching the shape of the gamma distribution.

Three specific cases (two QLCS cases and one supercell cluster case) are used to further investigate the results of the radar retrievals. Time series comparisons of the observed and radar retrieved rain parameters show relatively good agreement. Overall, the radar retrieval underestimates most rain parameters (relative to the disdrometer observations) during convective periods of rainfall, while the opposite is the case during stratiform rain. This suggests that there is a need to treat the retrieval differently based on the type of rainfall. Finally, the radar retrieval methods can be applied to entire radar sweeps, estimating microphysical parameters at high spatial resolutions yet over a much larger-scale than disdrometers are capable of measuring. The ability to retrieve microphysical parameters across entire radar sweeps is a valuable application that can provide a much more detailed look into the evolution of tornadic storms than what is currently available from limited *in-situ* measurements.

In the future, larger data sets are needed to increase statistical robustness of the retrieval of the μ-Λ relation and to increase the statistical significance of any derived relations. Targeted X-band radar measurements to compare with disdrometer observations would also be very beneficial in future work. X-band radars are able to gather radar data at much higher spatial and temporal resolutions, giving them the ability to observe data that would likely be more closely matched with disdrometer observations. Continued investigations into the various factors that may impact the accuracy of radar retrievals are also needed. Climatic regime, storm type, and storm phase may all play an important role in the ability of a retrieval method to accurately estimate microphysical parameters across large spatial scales, and methods will need to continue to be fine-tuned based on these factors.

7. REFERENCES

Ashley, W. S., 2007: Spatial and temporal analysis of tornado fatalities in the United States: 1880–2005. *Wea. Forecasting*, **22**, 1214-1228.

——, A. J. Krmenec, and R. Schwantes, 2008: Vulnerability due to nocturnal tornadoes. *Wea. Forecasting*, **23**, 795-807.

Atlas, D., R. C. Srivastava, and R. S. Sekhon, 1973: Doppler radar characteristics of precipitation at vertical incidence. *Rev. Geophys. Space Phys.*, **11**, 1–35.

——, and C. Ulbrich, 2006: Drop size spectra and integral remote sensing parameters in the transition from convective to stratiform rain. *Geophys. Res. Lett.*, **33**, 16.

Brandes, E. A., G. Zhang, and J. Vivekanandan, 2002: Experiments in rainfall estimation with a polarimetric radar in a subtropical environment. *J. Appl. Meteor.*, **41**, 674–685.

——, ——, and ——, 2003: An evaluation of a drop distribution–based polarimetric radar rainfall estimator. *J. Appl. Meteor.*, **42**, 652–660.

——, ——, and ——, 2004a: Drop size distribution retrieval with polarimetric radar: Model and application. *J. Appl. Meteor.*, **43**, 461–475.

——, ——, and ——, 2004b: Comparison of polarimetric radar drop size distribution retrieval algorithms. *J. Atmos. Ocean. Technol.*, **21**, 584–598.

Bringi, V. N., G. J. Huang, V. Chandrasekar, and E. Gorgucci, 2002: A methodology for estimating the parameters of a gamma raindrop size distribution model from polarimetric radar data: Application to a squall-line event from the TRMM/Brazil campaign. *J. Atmos. Ocean. Technol.*, **19**, 633–645.

——, V. Chandrasekar, J. Hubbert, E. Gorgucci, W. L. Randeu, and M. Schoenhuber, 2003: Raindrop size distribution in different climatic regimes from disdrometer and dual-polarized radar analysis. *J. Atmos. Sci.*, **60**, 354–365.

Cao, Q., G. Zhang, E. A. Brandes, T. Schuur, A. Ryzhkov, and K. Ikeda, 2008: Analysis of video disdrometer and polarimetric radar data to characterize rain microphysics in Oklahoma. *J. Appl. Meteor. Climatol.*, **47**, 2238–2255.

——, and ——, 2009: Errors in estimating raindrop size distribution parameters employing disdrometer and simulated raindrop spectra. *J. Appl. Meteor. Climatol.*, **48**, 406–425.

Chandrasekar, V., and V. N. Bringi, 1987: Simulation of radar reflectivity and surface measurements of rainfall. *J. Atmos. Ocean. Technol.*, **4**, 464–478.

Cressman, G. P., 1959: An operational objective analysis system. *Mon. Wea. Rev*, **87**, 367-374.

Davis, J. M., and M. D. Parker, 2014: Radar climatology of tornadic and nontornadic vortices in high-shear, low-CAPE environments in the mid-Atlantic and southeastern United States. *Wea. Forecasting*, **29**, 828-853.

Dawson, D. T., II, M. Xue, J. A. Milbrandt, and M. K. Yau, 2010: Comparison of evaporation and cold pool development between single-moment and multi-moment bulk microphysics schemes in idealized simulations of tornadic thunderstorms. *Mon. Wea. Rev.*, **138**, 1152-1171.

——, and G. Romine, 2011: A preliminary survey of DSD measurements conducted during VORTEX2. *25th Conference on Severe Local Storms*, 8A.4.

——, M. Xue, J. A. Milbrandt, and A. Shapiro, 2015: Sensitivity of real-data simulations of the 3 May 1999 Oklahoma City tornadic supercell and associated tornadoes to multimoment microphysics. Part I: Storm-and tornado-scale numerical forecasts. *Mon. Wea. Rev.*, **143**, 2241-2265.

——, ——, A. Shapiro, J. A. Milbrandt, and A. D. Schenkman, 2016: Sensitivity of real-data simulations of the 3 May 1999 Oklahoma City tornadic supercell and associated tornadoes to multimoment microphysics. Part II: Analysis of buoyancy and dynamic pressure forces in simulated tornado-like vortices. *J. Atmos. Sci.*, **73**, 1039–1061.

Friedrich, K., E. A. Kalina, F. J. Masters, and C. R. Lopez, 2013: Drop-size distributions in thunderstorms measured by optical disdrometers during VORTEX2. *Mon. Wea. Rev.*, **141**, 1182–1203.

Gertzman, H. S., and D. Atlas, 1977: Sampling errors in the measurements of rain and hail parameters. *J. Geophys. Res.*, **82**, 4955–4966.

Gilmore, M. S., J. M. Straka, and E. N. Rasmussen, 2004: Precipitation uncertainty due to variations in precipitation particle parameters within a simple microphysics scheme. *Mon. Wea. Rev.*, **11**, 2610–2627.

Gorgucci, E., V. Chandrasekar, V. N. Bringi, and G. Scarchilli, 2002: Estimation of raindrop size distribution parameters from polarimetric radar measurements. *J. Atmos. Sci.*, **59**, 2373–2384.

Gunn, R., and G. D. Kinzer, 1949: The terminal velocity of fall for water droplets in stagnant air. *J. Meteor.*, **6**, 243–248.

Guyer, J. L., and A. R. Dean, 2010: Tornadoes within weak CAPE environments across the continental United States. *25ᵗʰ Conf. on Severe Local Storms,* Denver, CO, Amer. Meteor. Soc., 1.5. [Available online at http://ams.confex.com/ams/pdfpapers/175725.pdf].

Haddad, Z. S., D. A. Short, S. L. Durden, E. Im, S. H. Hensley, M. B. Grable, and R. A. Black, 1997: A new parameterization of the rain drop size distribution. *IEEE Trans. Geosci. Remote Sens.*, **35** , 532–539.

Hunter, J. D., 2007: Matplotlib: A 2D graphics environment. *Computing in science & engineering*, **9**, 90-95.

Ishimari, A., 1991: Electromagnetic wave propagation, radiation, and scattering. Prentice Hall, 637 pp.

Jung, Y., G. Zhang, and M. Xue, 2008: Assimilation of simulated polarimetric radar data for a convective storm using the ensemble Kalman filter. Part I: Observation operators for reflectivity and polarimetric variables. *Mon. Wea. Rev.*, **136**, 2228-2245.

——, M. Xue, and G. Zhang, 2010: Simulations of polarimetric radar signatures of a supercell storm using a two-moment bulk microphysics scheme. *J. Appl. Meteor. Climatol.*, **49**, 146-163.

Kalina, E. A., K. Friedrich, S. M. Ellis, and D. W. Burgess, 2014: Comparison of disdrometer and X-band mobile radar observations in convective precipitation. *Mon. Wea. Rev.*, **142**, 2414–2435.

Kliche, D. V., P. L. Smith, and R. W. Johnson, 2008: L-moment estimators as applied to gamma drop size distributions. *J. Appl. Meteor. Climatol.,* **47**, 3117–3130.

Kozu, T., and K. Nakamura, 1991: Rain parameter estimation from dual-radar measurements combining reflectivity profile and path-integrated attenuation. *J. Atmos. Oceanic Technol.*, **8**, 259–270.

Kumjian, M. R., Z. J. Lebo, and H. C. Morrison, 2015: On the mechanisms of rain formation in an idealized supercell storm. *Mon. Wea. Rev.*, **143**, 2754-2773.

Laws, J. O., and D. A. Parsons, 1943: The relationship of raindrop size to intensity. *Trans. Amer. Geophys. Union*, **24**, 452–460.

Lee, G., and I. Zawadzki, 2005: Variability of drop size distributions: Time-scale dependence of the variability and its effects on rain estimation. *J. Appl. Meteor.*, **44**, 241–255.

Löffler-Mang, M., and J. Joss, 2000: An optical disdrometer for measuring size and velocity of hydrometeors. *J. Atmos. Ocean. Technol.*, **17**, 130–139.

Marshall, J. S., and W. M. Palmer, 1948: The size distribution of raindrops. *Q. J. R. Meteorol. Soc.*, **76**, 16–36.

——, 1953: Precipitation trajectories and patterns. *J. Meteor.*, **10**, 25-29.

McFarquhar, G. M., R. List, D. R. Hudak, R. P. Nissen, J. S. Dobbie, N. P. Tung, and T. S. Kang, 1996: Flux measurements of pulsating rain with a disdrometer and Doppler radar during Phase II of the Joint Tropical Rain Experiment in Malaysia. *J. Appl. Meteor.*, **35**, 859-874.

Park, S. G., H. L. Kim, Y. W. Ham, and S. H. Jung, 2017: Comparative evaluation of the OTT PARSIVEL2 using a collocated two-dimensional video disdrometer. *J. Atmos. Ocean. Technol.*, **34**, 2059–2082.

Rasmussen, E., 2015: VORTEX-Southeast program overview. *NSSL Tech. Report*, 36pp.

Raupach, T. H., and A. Berne, 2015: Correction of raindrop size distributions measured by Parsivel disdrometers, using a two-dimensional video disdrometer as a reference. *Atmos. Meas. Tech.*, **8**, 343–365.

Rinehart, R. E., 2004: Radar for Meteorologists. Rinehart Publications, 482 pp.

Sauvageot, H., and M. Koffi, 2000: Multimodal raindrop size distributions. *J. Atmos. Sci.*, **57**, 2480–2492.

Schneider, R. S., A. R. Dean, S. J. Weiss, and P. D. Bothwell, 2006: Analysis of estimated environments for 2004 and 2005 severe convective storm reports. *23rd Conf. on Severe Local Storms,* St. Louis, MO, Amer. Meteor. Soc., 3.5. [Available online at http://ams.confex.com/ams/pdfpapers/115246.pdf].

Seliga, T. A., and V. N. Bringi, 1976: Potential use of radar differential reflectivity measurements at orthogonal polarizations for measuring precipitation. *J. Appl. Meteor.*, **15**, 69–76.

Sherburn, K. D., and M. D. Parker, 2014: Climatology and ingredients of significant severe convection in high-shear, low-CAPE environments. *Wea. Forecasting*, **29**, 854-877.

Smith, P. L., D. V. Kliche, and R. W. Johnson, 2005: The bias in moment estimators for parameters of drop-size distribution functions: Sampling from gamma distributions. Preprints, 32nd

Conf. on Radar Meteorology, Albuquerque, NM, Amer. Meteor. Soc., 15R. 5. [Available online at http://ams.confex.com/ams/ pdfpapers/97018.pdf].

Snook, N., and M. Xue, 2008: Effects of microphysical drop size distribution on tornadogenesis in supercell thunderstorms. *Geophys. Res. Lett.*, **35,** L24803.

Thurai, M., W. A. Petersen, A. Tokay, C. Schultz, and P. Gatlin, 2011: Drop size distribution comparisons between Parsivel and 2-D video disdrometers. *Adv. Geosci.*, **30**, 3–9.

——, C. R. Williams, and V. N. Bringi, 2014: Examining the correlations between drop size distribution parameters using data from two side-by-side 2D-video disdrometers. *Atmos. Res.*, **144**, 95–110.

Tokay, A., and D. A. Short, 1996: Evidence from tropical raindrop spectra of the origin of rain from stratiform versus convective clouds. *J. Appl. Meteor.,* **35***,* 355–371.

——, A. Kruger, and W. Krajewski, 2001: Comparison of drop size distribution measurements by impact and optical disdrometers, *J. Appl. Meteor.*, **40**, 2083–2097.

——, W. A. Petersen, P. Gatlin, and M. Wingo, 2013: Comparison of raindrop size distribution measurements by collocated disdrometers, *J. Atmos. Ocean. Technol.*, **30**, 1672–1690.

——, D. B. Wolff, and W. A. Petersen, 2014: Evaluation of the new version of the laser-optical disdrometer, OTT Parsivel 2. *J. Atmos. Ocean. Technol.*, **31**, 1276–1288.

Ulbrich, C. W., 1983: Natural variations in the analytical form of the raindrop size distribution. *J. Climate Appl. Meteor.*, **22**, 1764–1775.

——, 1985. The effects of drop size distribution truncation on rainfall integral parameters and empirical relations. *J. Appl. Meteor. Climatol.* **24**, 580–590.

——, and D. Atlas, 1998: Rainfall microphysics and radar properties: Analysis methods for drop size spectra. *J. Appl. Meteor.*, **37**, 912–923.

Vivekanandan, J., W. M. Adams, and V. N. Bringi, 1991: Rigorous approach to polarimetric radar modeling of hydrometeor orientation distributions. *J. Appl. Meteor.*, **30**, 1053–1063.

——, G. Zhang, and E. Brandes, 2004: Polarimetric radar estimators based on a constrained gamma drop size distribution model. *J. Appl. Meteor.* **43**, 217–230.

Waterman, P. C., 1969: Scattering by dielectric obstacles. *Alta Freq.*, **38**, 348–352.

Wong, R. K. W., and N. Chidambaram, 1985: Gamma size distribution and stochastic sampling errors. *J. Appl. Meteor.*, **24**, 568–579.

Zhang, G., J. Vivekanandan, and E. A. Brandes, 2001: A method for estimating rain rate and drop size distribution from polarimetric radar measurements. *IEEE Trans. Geosci. Remote Sens.*, **39**, 830–841.

——, ——, ——, R. Meneghini, and T. Kozu, 2003: The shape-slope relation in observed gamma raindrop size distributions: Statistical error or useful information? *J. Atmos. Ocean. Technol.*, **20**, 1106–1119.

——, J. Sun, and E. A. Brandes, 2006: Improving parameterization of rain microphysics with disdrometer and radar observations. *J. Atmos. Sci.*, **63**, 1273–1290.

——, M. Xue, Q. Cao, and D. Dawson, 2008: Diagnosing the intercept parameter for exponential raindrop size distribution based on video disdrometer observations: Model development. *J. Appl. Meteorol. Climatol.*, **47**, 2983–2992.

——. Subroutine of DSD retrieval source code. [Available online at https://arrc.ou.edu/~guzhang/Polarimetry/datacode.htm].